

ABSTRACT

THERMAL AND STRUCTURAL ANALYSIS OF BEAMLINE COMPONENTS IN THE MU2E EXPERIMENT

Luke D. Martin, M.S.
Department of Mechanical Engineering
Northern Illinois University, 2016
Dr. Nicholas Pohlman, Director

Fermi National Accelerator Laboratory will be conducting the high energy particle physics experiment Muons to Electrons (Mu2e). In this experiment, physicists will attempt to witness and understand an ultra-rare process which is the conversion of a muon into the lighter mass electron, without creating additional neutrinos. The experiment is conducted by first generating a proton beam which will be collided into a target within the production solenoid (PS). This creates a high intensity muon beam which passes through a transport solenoid (TS) and into the detector solenoid (DS). In the detector solenoid the muons will be stopped in an aluminum target and a series of detectors will measure the electrons produced. These components have been named the DS train since they are coupled and travel on a rail system when being inserted or extracted from the DS. To facilitate the installation and removal of the DS train, a set of external stands and a support stand for the instrumentation feed-through bulkhead (IFB) have been designed. Full analysis of safety factors and performance of these two designs has been completed. The detector solenoid itself will need to be maintained to a temperature of $22^{\circ}\text{C} \pm 10^{\circ}\text{C}$. This will minimize thermal strain and ensure the accurate position of the components is maintained to the tolerance of ± 2 mm. To reduce the thermal gradient, a passive heating system has been developed and reported.

NORTHERN ILLINOIS UNIVERSITY
DE KALB, ILLINOIS

MAY 2016

THERMAL AND STRUCTURAL ANALYSIS OF BEAMLINER COMPONENTS IN THE
MU2E EXPERIMENT

BY

LUKE D. MARTIN
© 2016 Luke D. Martin

A THESIS SUBMITTED TO THE GRADUATE SCHOOL
IN PARTIAL FULFILLMENT OF THE REQUIREMENTS
FOR THE DEGREE
MASTER OF SCIENCE

DEPARTMENT OF MECHANICAL ENGINEERING

Thesis Director:
Dr. Nicholas Pohlman

ACKNOWLEDGEMENTS

I would like to thank the Department of Energy, the National Science Foundation, and Fermi National Accelerator Laboratory for their collaboration with Northern Illinois University on the Mu2e experiment. I am grateful for the opportunity to contribute to such a large scale project and develop my professional skills. I would like to especially thank muon beamline group for their involvement and guidance in my research. Rodger Bossert, Jeff Brandt, Giuseppe Gallo, Tom Page, Kurt Krempetz, Tom Nicol, Horst Friedman, and George Ginther, your advice and guidance in solving engineering problems has greatly contributed to advancing my engineering abilities. Dr. Pohlman I am grateful for your continued support both in directing this thesis and as a supervisor the for last 3 year. Dr. Hedin and Dr. Majumdar thank you for serving on my graduate thesis committee and providing me with guidance on this research project.

DEDICATION

To my wonderful wife Kayla Joy Martin. Your support, love, and patience
has made completing this thesis possible.

TABLE OF CONTENTS

	Page
List of Tables	viii
List of Figures.	ix
Chapter	
1 Introduction.	1
1.1 Physics Motivation of the Mu2e Experiment	1
1.1.1 Particle Physics Theory.	1
1.2 Experiment Overview	3
1.3 Mu2e Solenoids.	4
1.3.1 Production Solenoid (PS)	4
1.3.2 Transport Solenoid (TS)	5
1.3.3 Detector Solenoid (DS)	6
1.3.3.1 DS Rail System.	8
1.4 Thesis Objective	10
2 Instrumentation Feedthrough Bulkhead Support	12
2.1 Role of the IFB support.	12
2.2 Design Specifications	13
2.2.1 Structural Requirements	14
2.2.2 Spatial and Positional Requirements.	14

Chapter	Page
2.3 Structural Analysis	15
2.3.1 Insertion Finite Element Analysis.	16
2.3.1.1 Analysis Conditions.	16
2.3.1.2 Deformation	17
2.3.1.3 Stress.	18
2.3.2 Extraction Finite Element Analysis	19
2.3.2.1 Analysis Conditions.	19
2.3.2.2 Deformation	20
2.3.2.3 Stress.	20
2.3.3 Design Status Summary	21
3 External Stands	22
3.1 Role of the External Stands	22
3.2 Design Specifications	23
3.2.1 Geometric and Spacial Requirements	23
3.2.2 Magnetic Requirements.	24
3.2.3 Structural Requirements	24
3.3 Analytical Analysis	24
3.3.1 Maximum Deflection Loading Parameters	25
3.3.2 Centroid Calculations	27
3.3.2.1 Aluminum Centroid.	27
3.3.2.2 HPM75 and Standard Steel Rail Centroid Calculations.	29
3.3.2.3 Neutral Axis Calculations	29
3.3.3 Area Moment of Inertia and Weighted Flexural Rigidity Calculations	31
3.3.4 Deflection	32

Chapter	Page
3.3.5 Stress	34
3.4 Finite Element Analysis.	36
3.4.1 Loading Conditions.	36
3.4.2 Total Deformation	37
3.4.3 Vertical Deformation.	38
3.4.4 Stress	39
3.4.5 Safety Factor	40
3.5 Mock Up Testing.	41
3.5.0.1 Adjustment Methodology.	42
3.5.0.2 Adjustment Results.	44
3.6 Design Status Summary.	45
4 Detector Solenoid Thermal Control	46
4.1 Purpose of a Thermal Management System	46
4.2 Heat Transfer	47
4.2.1 Preliminary DS Finite Element Analysis.	48
4.2.1.1 Boundary Conditions.	48
4.2.1.2 Temperature Distribution.	49
4.2.2 Secondary DS Finite Element Analysis.	50
4.2.2.1 Thermal Boundary Conditions	50
4.2.2.2 Temperature Distribution.	51
4.2.2.3 Structural Boundary Conditions	51
4.2.2.4 Deformation	52
4.2.2.5 Stress along Rail	55

Chapter	Page
4.3 Model Validation.	56
4.3.1 Comparison	57
4.3.2 Necessity of Temperature Control.	58
4.3.2.1 Geometric Constraints	58
4.3.2.2 Magnetic Constraints.	59
4.3.2.3 Temperature Requirements	59
4.3.3 Preliminary Passive Heating System Finite Element Analysis	60
4.3.3.1 Copper Geometry	60
4.3.3.2 Thermal Boundary Conditions	60
4.3.3.3 Temperature Distribution.	62
4.4 Design Status Summary.	62
References.	64
Appendix: External Stand Drawings	66

LIST OF TABLES

Table	Page
3.1 Aluminum centroid calculations	28
3.2 Area moment of inertia calculations	31
4.1 DS geometry.	47

LIST OF FIGURES

Figure	Page
1.1 The standard model showing spin, electrical charge, and mass properties [2].	2
1.2 Fermilab accelerator complex [4].	3
1.3 The production solenoid (4 m), transport solenoid (13 m), and detector solenoid (11 m) [5].	4
1.4 The PS, note the beam entering on the right via the pipe [6].	5
1.5 The transport solenoid [5]	6
1.6 The detector solenoid (operational position) [5]	7
1.7 Internal rail system design [11].	9
1.8 Detector solenoid components outside of the bore (maintenance position) [11]	10
2.1 IFB (blue) and IFB support (gray).	12
2.2 IFB-trunnion connection upstream (left) to downstream (right) [10]	13
2.3 IFB analysis loading conditions	16
2.4 IFB insertion deformation	17
2.5 IFB insertion stress	18
2.6 IFB analysis conditions	19
2.7 IFB extraction deformation	20
2.8 IFB extraction stress	21
3.1 Completed iteration 2 design of the external stands	22
3.2 Loading schematic [14].	25

Figure	Page
3.3 Calorimeter load (left two black arrows), MBS load (right two black arrows) centered load (blue).	26
3.4 Beam cross-sectional view	28
3.5 Moment of inertia for steel, aluminium, and combined	30
3.6 Theoretical deflections compared to FEA	33
3.7 Theoretical internal moment for the external stands.	35
3.8 External stand loads from tracker, calorimeter, and gravity.	37
3.9 External stands total deformation.	38
3.10 External stand vertical deformation	38
3.11 External stand von-mises stress	39
3.12 External stand safety factor	40
3.13 External stand mock up.	41
3.14 External stand adjustment region	42
3.15 External stand measurements large cones (before loading), small cones (after loading)	44
4.1 Simplified scheme of the solenoid and vessel.	48
4.2 Boundary conditions and load in vacuum with symmetry imposed.	49
4.3 Temperature distribution in half of the model of the DS.	49
4.4 Boundary conditions and load in vacuum	50
4.5 Steady state temperature distribution	51
4.6 Boundary condition: displacement constraints	52
4.7 Total deformation from thermal contraction	52
4.8 Transverse deformation from thermal contraction.	53
4.9 Vertical deformation from thermal contraction.	53

Figure	Page
4.10 Axial deformation from thermal contraction	54
4.11 DS displacement of individual components	55
4.12 Stress along the rail from thermal contraction	55
4.13 Stress from thermal contraction	56
4.14 Comparison between theoretical and finite element solution	57
4.15 Cross-sectional view of the DS [11]	59
4.16 Geometry of with copper bars	61
4.17 Thermal boundary conditions.	61
4.18 Temperature distribution with copper bars	62

CHAPTER 1

INTRODUCTION

1.1 Physics Motivation of the Mu2e Experiment

High energy physicists have been actively studying particle interactions for years searching for evidence of interactions that lie beyond the standard model. Experimentation and investigation in this field will help scientists discover answers to fundamental questions about matter and the universe. One area of potential discovery during the next few decades will be research at the Intensity Frontier on ultra-rare processes, including the muon to electron conversion. Observing processes such as $\mu + N \rightarrow e + N$ and $\mu \rightarrow e + \gamma$ conversions will remove a hurdle to understanding the relationship among the three generations of leptons (electrons, muons, and taus) and possibly the origin of matter-antimatter asymmetries. Exploration into these unknowns could expand the understanding of phenomena that play an integral role in the universe [1].

1.1.1 Particle Physics Theory

The standard model of particle physics is a theory that classifies all of the known subatomic particles and explains particle interactions. The model contains the 24 fundamental fermions, which are 12 particles and their anti-particle counterparts, as well as 6 bosons. The fermions are divided into two groups: quarks and leptons and make up the matter in the universe. The bosons are responsible for electromagnetic, weak, and strong forces, and

through the Higgs boson, the masses of particles. The W and Z bosons are exchange particles of the weak force. The weak force explains things such as the energy production in the sun and is responsible for radioactive beta decay. The strong interaction acts on the quarks. The force carrier is the gluon, which holds together the quarks in the neutrons and protons and even holds the nucleus together. The electromagnetic force includes interactions of charged particles and the force carrier is the photon.

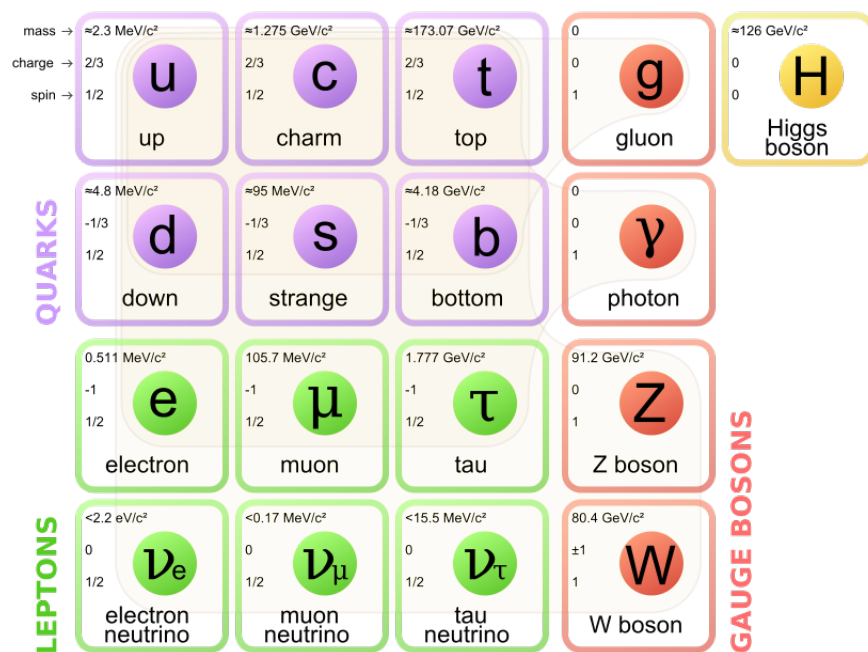


Figure 1.1: The standard model showing spin, electrical charge, and mass properties [2]

With the observation that neutrinos oscillate from one flavor to another, verifying that the neutrinos are not massless, the standard model predicts that muons will convert into electrons. However, due to the very small mass of neutrinos, the predicted standard model rate of neutrinoless conversion of muons to electrons is extremely suppressed and is essentially unobservable. The normal muon decay is $\mu^- \rightarrow e^- + \nu_\mu + \bar{\nu}_e$. This transition conserves the muon and electron number. However, the signal for Mu2e is $\mu^- + N \rightarrow e^- + N$ which violates the lepton number decay and is a charged lepton flavor violation. The search for evidence

of lepton number violation began soon after the discovery of the muon, and observing it in this channel would provide insight into new areas of physics.

1.2 Experiment Overview

The Mu2e experiment will be conducted at the Fermilab campus in Batavia, IL. The main injector (proton accelerator) for the Mu2e experiment is already built and is commonly used for numerous experiments at Fermilab. A separate beamline and Mu2e building must be built. Currently, the construction is underway and is expected to ongoing until the year 2020. The experimental system is currently being designed and will provide researchers with 10,000 times more data than previous experiments [3].

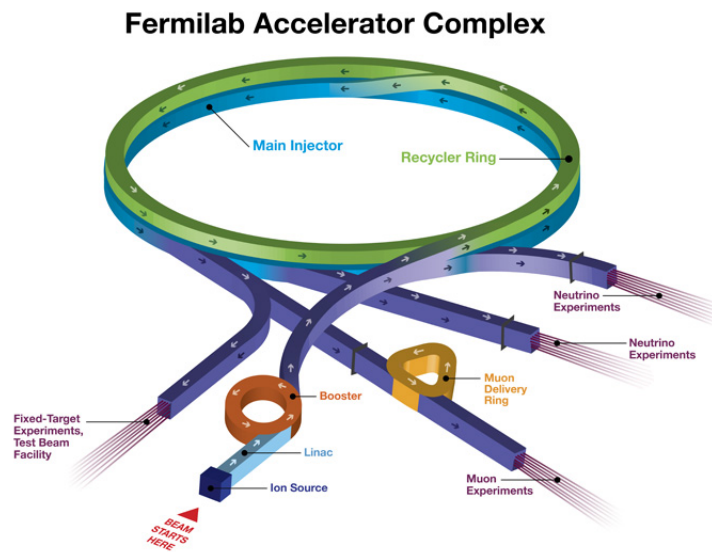


Figure 1.2: Fermilab accelerator complex [4]

1.3 Mu2e Solenoids

The solenoids in the Mu2e experiment are used to produce and transport muons to an aluminum target where a significant fraction of those muons are stopped. This provides an opportunity to observe the muon to electron conversion. Figure 1.3 shows a top view of the three solenoids. The solenoids are connected and each have highly controlled environments that manipulate the beam.

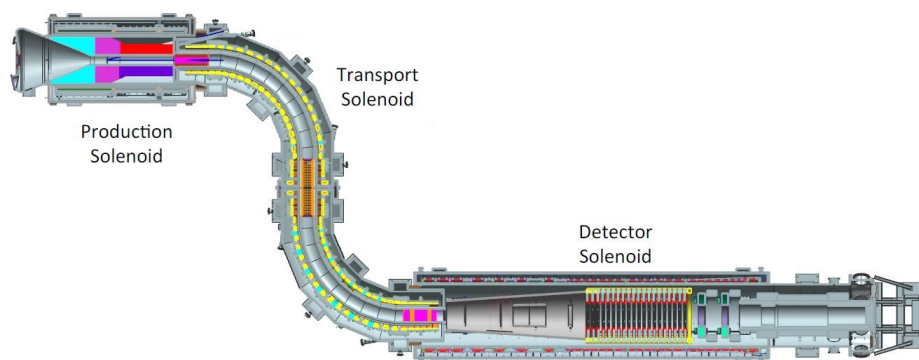


Figure 1.3: The production solenoid (4 m), transport solenoid (13 m), and detector solenoid (11 m) [5]

1.3.1 Production Solenoid (PS)

The production solenoid as the name implies is used to produce muons. Inside the production solenoid is a tungsten target. A proton beam is generated and accelerated by the main injector (see Figure 1.2), manipulated into a tuned bunch structure with a bunch separation of 1695 nanoseconds in the muon delivery ring, and then directed into the target located in the center of the PS. When the beam hits the target there are many particles produced, some of which are charged pions which decay into muons. The protons which do

not interact in the target will leave the PS bore through the end cap and are absorbed by the PS beam dump. The muon beam is directed into the transport solenoid.

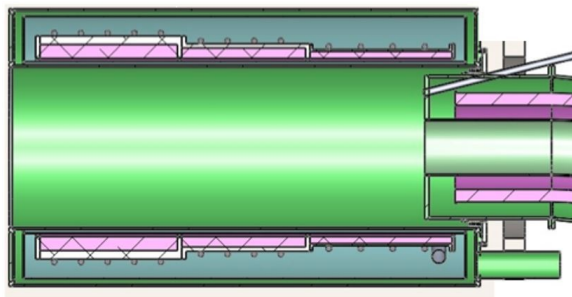


Figure 1.4: The PS, note the beam entering on the right via the pipe [6]

1.3.2 Transport Solenoid (TS)

The primary function of the transport solenoid is to supply the detector solenoid with a low momentum negatively-charged muon beam from the production solenoids. The transport solenoid consists of five sectors label TS1→ TS5, see Figure 1.5. It is separated into an upstream and a downstream section, with TSu (transport solenoid upstream) comprised of TS1, TS2, and half of TS3, while TSd (transport solenoid downstream) includes the second half of TS3, TS4, and TS5.

The PS magnetic field is designed to decrease from the upstream end to the downstream end. The purpose of this design is to minimize risk of trapping charged particles. Once the beam enters the first curved section, TS2, it is dispersed and a collimator selects particles based on their sign and momentum [7]. TS3 maintains the momentum of the particles as they pass through and enter TS4. Once inside TS4 the muon particles converge and become aligned with the center of TS5. TS5 is aligned with the stopping target in the DS and transports the beam out of the TS and into the DS.

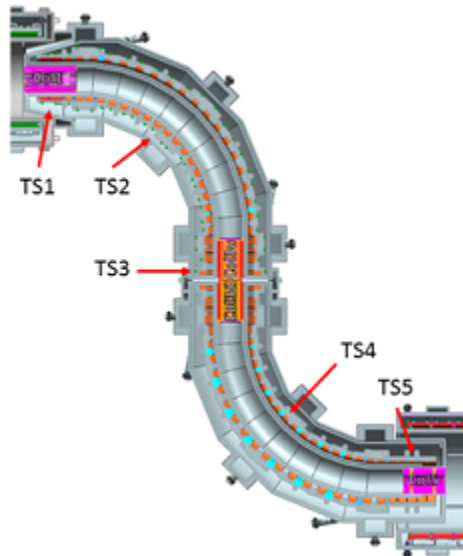


Figure 1.5: The transport solenoid [5]

1.3.3 Detector Solenoid (DS)

The detector solenoid is the last solenoid used in the Mu2e experiment. It is also the location where the direct muon to electron conversion search will occur. The DS is comprised of two concentric tubes. The region between the inner shell and the outer shell contains the superconducting magnet which generates the 1-2 Tesla magnetic field that exists axially along the DS. The inner bore (also known as the warm bore) of the DS is 10900 mm in length and has an inner diameter of 1900 mm. The region between the cylinders contains a liquid nitrogen intercept that will be cooled to 80K. The solenoid coil will only be superconducting when the temperature of the coil is much closer to 5K. The cold mass is cooled to this temperature using liquid helium. To reduce radiative heat loss from the room temperature inner bore and the 80K intercept, 45 sheets of multilayer insulation (MLI) will be added. Analyses reported in Chapter 4 show the even with the MLI thermal shield, a thermal control system will need to be used in the warm bore.

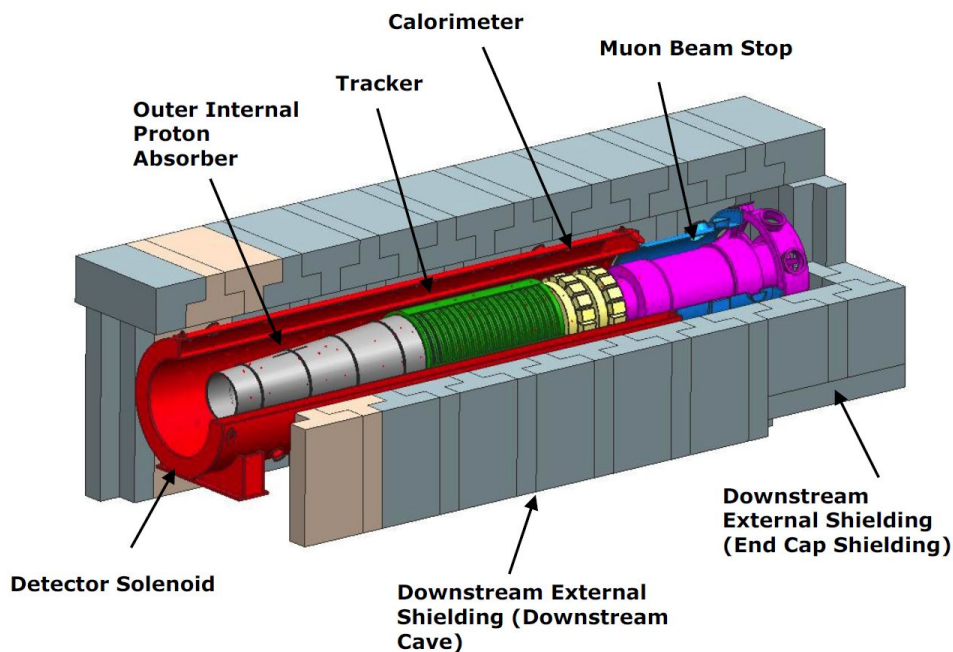


Figure 1.6: The detector solenoid (operational position) [5]

The first component that the muon beam will encounter when entering the DS is the muon stopping target which is located at the center of the proton absorber. After the beam hits the target, approximately 40% [8] of the muons are stopped. These muons are stopped in the target nuclei and then either decay in orbit or are captured by the aluminum nucleus and produce various byproducts such as electrons, neutrons, protons, neutrinos, and gamma rays. However, there is also a conversion where the $\mu^- + Al \rightarrow e^- + Al$ reaction occurs which this is the “signal reaction” whose search is the study of this experiment.

About 15% of the time that a muon is captured a proton is emitted with an energy spectrum center at 7 MeV [9]. These protons generate background in the tracker, and contribute to the aging of the detector. This causes the need for a proton absorber. There are two proton absorbers surrounding the stopping target and they both are used to reduce the momentum of protons which enter the tracker.

The next component the beam passes through is the tracker. The tracker is responsible for measuring the trajectory and momentum of the charged particles. After this is the calorimeter identifies that a particle is an electron and provides a measurement of its energy. The data from the tracker and calorimeter is used to identify the electrons which originate from interacting with the stopping target.

The final component in the detector solenoid is the muon beam stop (MBS), where the remaining 60% of the muons stop. The purpose of the MBS is to absorb the energy of beam particles and minimize the noise to the detectors that occurs from the muon decays. The detectors are the tracker, calorimeter, and a cosmic ray veto counts which cover the upper 3/4 of the DS cryostat. The muon beamstop consists of a stainless steel tube that has concentric tubes of high density polyethylene throughout the interior as well as over a portion of the outer surface. A series of cut outs have been placed in the bottom to increase gas flow when the DS is being pumped to high vacuum. Additionally, an end plug has been added at the downstream end of the beam to stop muons at small radii.

On the upstream side the muon beam stop is connected to a support called the spherical support which was designed to offer freedom of movement in the back end of the MBS [10]. On the downstream side it is attached to the instrumentation feedthrough bulkhead (IFB) and IFB support, see Figure 1.8. The IFB support structure that will carry approximately 50% of the MBS weight will be discussed in detail in Chapter 2.

1.3.3.1 DS Rail System

The detector solenoid is unique among the solenoids due to the fact that the internal components need to be removed periodically for servicing. To accomplish this task a rail system has been developed. The system is broken into two parts: internal and external. The

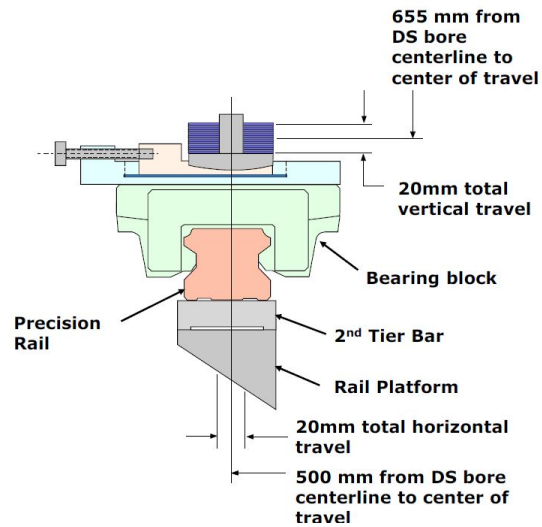


Figure 1.7: Internal rail system design [11]

internal rails are bolted into platforms at the bottom of the DS and separated by 1000 mm center to center. The detector solenoid components are attached to bearing blocks which roll along the rails. The components on the master rail side remain in a fixed position relative to the bearing blocks. Alternatively, the component attachment to the bearing blocks on the slave rail side is “floating” and allows relative movement (between the component and bearing block) in the transverse direction. A view of one side is shown in Figure 1.7, where the rail platform is attached to the DS bore by longitudinal welds. The external rail system consists of 6 aluminum stands and the bearing block rails which bolt to the top of them, see Figure 1.8. The DS bore is a considerable height from the floor, and the external stands bridge the distance from the floor to the rails. The stands provide the support for the detector solenoid train when it is in the maintenance position as shown in Figure 1.8. The stands will be discussed in further detail in Chapter 3.

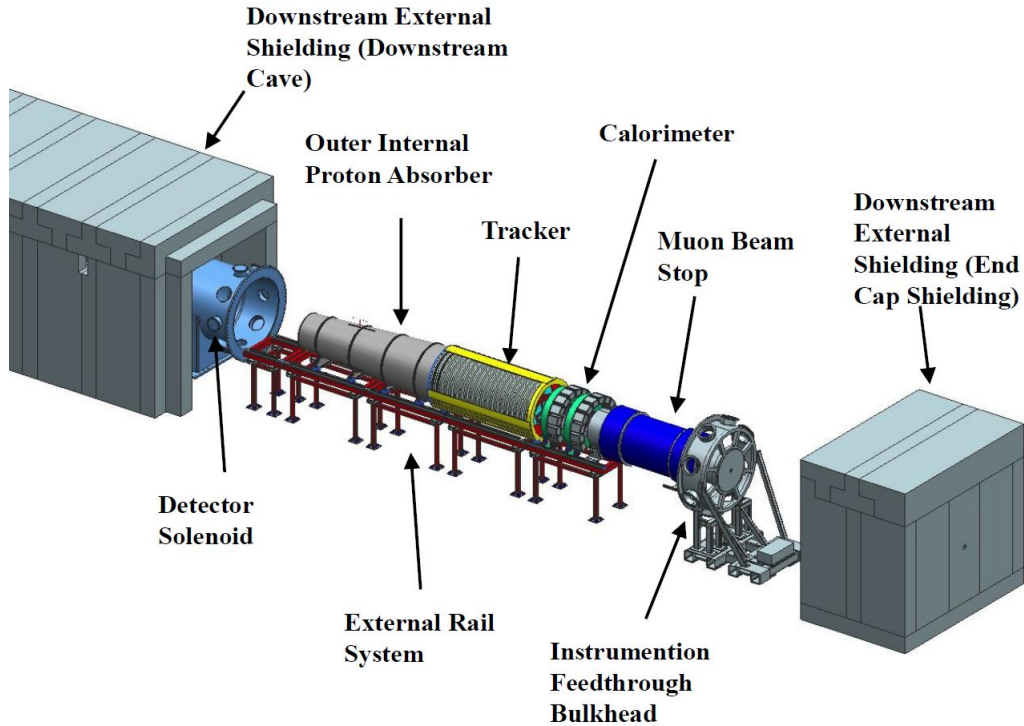


Figure 1.8: Detector solenoid components outside of the bore (maintenance position) [11]

1.4 Thesis Objective

The objective of this thesis is to a) design and analyze the external stands and the instrumentation feedthrough bulkhead, and b) develop a thermal management system to maintain the temperature of the DS warm bore near 22 °C. All of these designs will be used for the lifetime of the Mu2e experiment. Many requirements have been imposed on each of the designs due to environment, geometry, and safety codes. Potential failure methods are considered and addressed. For the external stands and IFB support, prototypes will be ordered and tested.

Chapter 2 is focused on the IFB support design. Constraints and requirements are addressed, and a detailed structural analysis is shown. Chapter 3 describes the external stand design. It also includes both analytical and finite element analyses, as well as alignment

studies that were performed with the prototype. In Chapter 4 the justification of the need for heaters will be addressed, and a design is presented. The analytical and finite element methods to validate and optimize the design are shown.

CHAPTER 2

INSTRUMENTATION FEEDTHROUGH BULKHEAD SUPPORT

2.1 Role of the IFB support

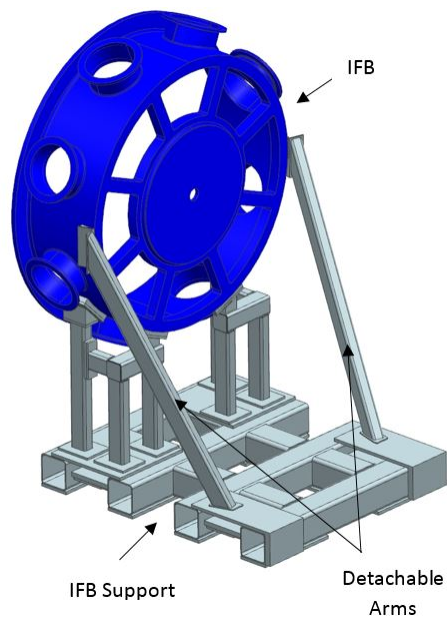


Figure 2.1: IFB (blue) and IFB support (gray)

The instrumentation feedthrough bulkhead (IFB), shown in Figure 2.1, is a welded 316L stainless steel cylindrical shell with a flange welded at one end. The purpose of the IFB is mate with the detector solenoid warm bore to create a vacuum seal. To power the components inside the solenoid cut outs have been made in the steel and replaced with instrumentation panel and port feedthroughs. These instrumentation feedthroughs provide location for power

cables, optical fibers, gas lines, and cooling lines to enter the high vacuum solenoid without creating a leak.

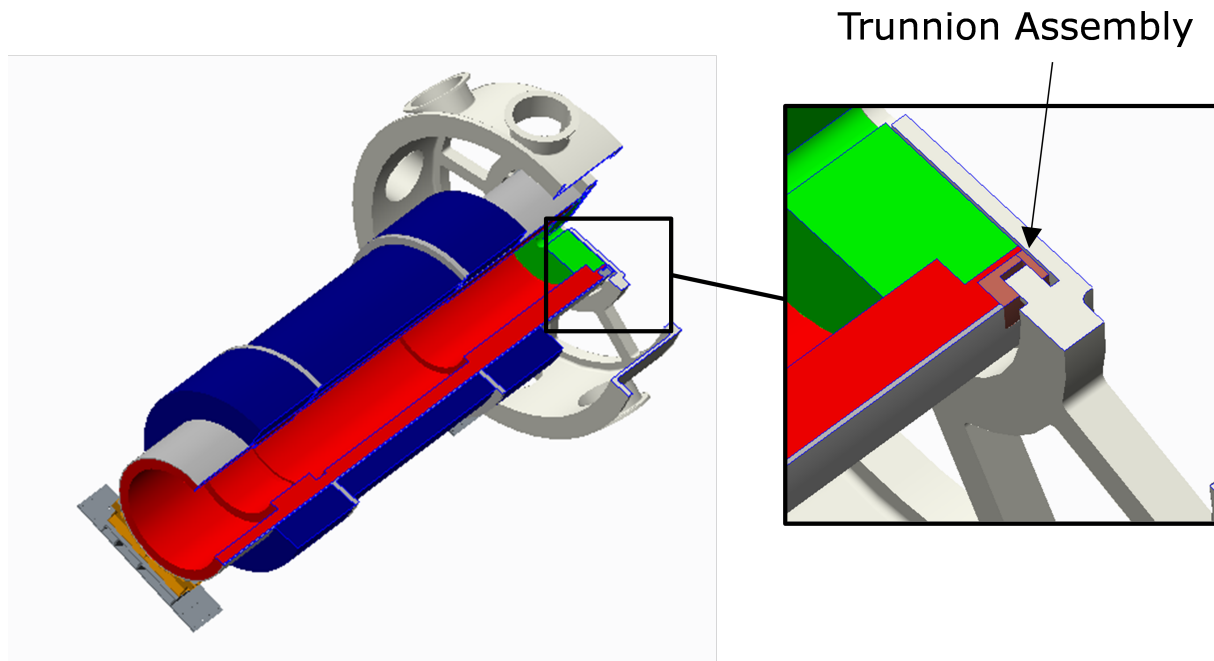


Figure 2.2: IFB-trunnion connection upstream (left) to downstream (right) [10]

The IFB connects to the DS train through a pair of trunnions that interlock with the muon beam stop. The connection between the IFB trunnions and the muon beam stop sockets can be seen in Figure 2.2. The IFB support is the mechanism that translates force as the DS train is installed and removed from the DS, see Figure 1.8.

2.2 Design Specifications

Various requirements have been developed and will continue to evolve for the IFB and IFB support as the Mu2e experiment progresses. Currently, the design is in the preliminary design 2 phase which includes sufficient space for the calorimeter and tracker cables. As the

details of the final designs for active components in the DS (tracker and calorimeter) are completed, the IFB support will undergo another design phase prior to production.

2.2.1 Structural Requirements

The primary function of the IFB support is to carry the gravitational load of the IFB. Since the structural support of the muon beam stop is shared by the rail system and the IFB, the IFB support must be able to withstand this additional load and meet adequate safety factor.

2.2.2 Spatial and Positional Requirements

The IFB support is designed so that it does not interfere with the vacuum pumpout spool piece (VPSP) ports or the VPSP support which is welded to the downstream end of the DS. The design must also fit within the end cap shielding, which encloses the area surround the DS. To achieve this, the bolted diagonal supports, depicted in Figure 2.1, are detachable. Additionally, relief channels have been put into the back of the end cap shielding. This allows the IFB support base to fit underneath the downstream end of the concrete enclose. Another aspect of the design is that the final attached position of the IFB must be extremely precise in order to create a close vacuum seal. This is of critical importance since the detector train components must be aligned to be ± 2 mm from their nominal position. Methodology for for final alignment is still being studied.

2.3 Structural Analysis

The current design for installing the IFB, IFB support, and detector train is to use two hydraulic cylinders to push on the base of the IFB support. Since the length to install the train is approximately 14000 millimeters, and the stroke of the cylinders is much smaller, the following method will be used.

1. The hydraulic cylinders are attached to the base of the IFB support.
2. The hydraulic cylinders are bolted into tapped holes in the steel floor plates.
3. Pressure is applied and the cylinders extended to their full stroke length, driving the train axially with respect to the DS.
4. Remaining attached to the IFB support, the cylinders are unbolted from the floor plates and compressed.
5. The cylinders are moved to the next upstream (or downstream for extraction) location.
6. Steps 2-5 are repeated until the train is fully installed or removed.

A critical aspect of analyzing the strength of the IFB support was to determine the required force to move the whole system into and out of the DS warm bore. The force that the cylinders must provide is equal to the force overcome the friction between the rails and the detector train as well as the hillman rollers and the steel track on which they roll. Presently, the calculated maximum load that the cylinders can apply is 4.5 kN per side [12].

One critical aspect that the design must satisfy is to not tip or be over stressed if the DS train came to a complete stop during installation. This could occur if the bearing blocks and rails became bound. In this arrangement the DS train (including the IFB) would be

constrained from moving axially to the DS, additional details are provided in the following sections.

2.3.1 Insertion Finite Element Analysis

This analysis is focused on validating the structural integrity of the IFB support using the worst case loading conditions during the insertion procedure. The case analyzed is a simulation of installing the train and assuming that one (or more) of a DS train component bearing blocks binds to the rails, halting the motion of the train and IFB.

2.3.1.1 Analysis Conditions

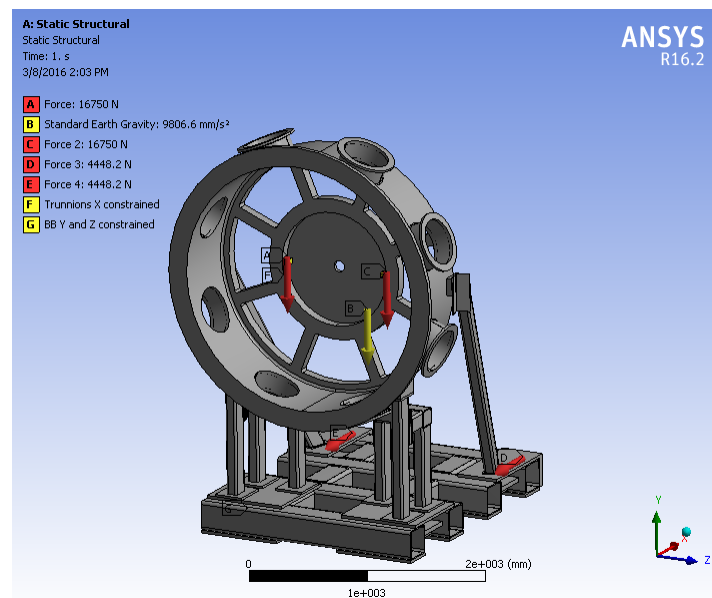


Figure 2.3: IFB analysis loading conditions

In this arrangement the hydraulic cylinders will be applying the maximum load (condition A and C) in the upstream direction to the base of the IFB support. Additionally, the

gravitational load of the IFB (condition B) and muon beam stop (condition D and E) is applied as well. To simulate the degrees of freedom of the rollers and trunnions displacement constraints have been applied. The trunnions are constrained in the axial direction (condition F) due to the nature of the connection between the trunnions and the muon beam stop socket, and free to move in the lateral and vertical direction. Alternatively, the 4 hillman roller locations have been constrained in the vertical and lateral directions (condition G) since they provide vertical support and are unable to roll laterally. They have been set to free in the axial direction, which is the direction they naturally roll.

2.3.1.2 Deformation

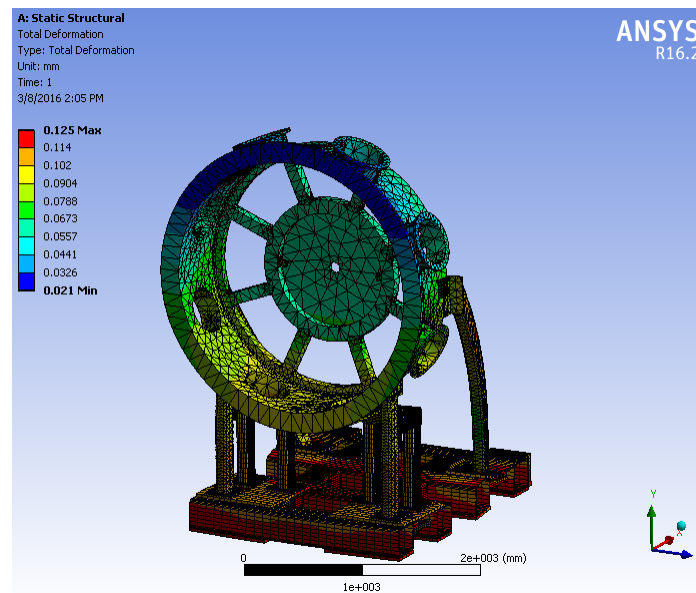


Figure 2.4: IFB insertion deformation

The deformation shown here is the magnitude throughout the support. It is important to note that this deformation is in the elastic range, so once the structure is unloaded it will return to its original shape. For the purpose of showing high deflection areas, the scale of

deformation is amplified by the software. It can be observed that the diagonal arms bow in response to the loads, thus the need for having them on the support during installation is justified. As can be expected the highest deformation occurs in the base along the line that the force acts in.

2.3.1.3 Stress

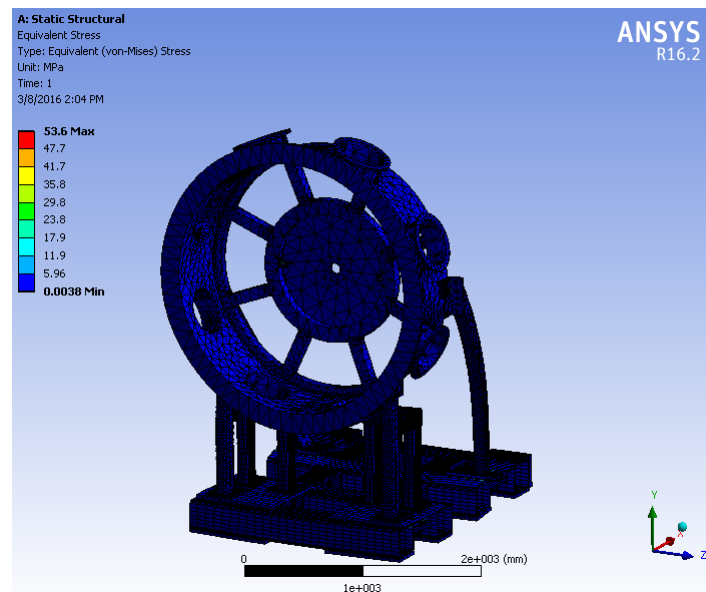


Figure 2.5: IFB insertion stress

The stress analyzed in this case is the von-mises stress, and it is used to calculate the safety factor of the design. The stresses seen in Figure 2.5 are rather minimal and reach approximately 53.6 MPa in joints and near the trunnions. The stress seen in this analysis is far less than the yield stress of 248 MPa for 316L stainless steel [10], providing a safety factor of 4.62.

2.3.2 Extraction Finite Element Analysis

This analysis will determine the strength of the IFB support during an extraction procedure. Worst potential conditions will be simulated as before, but with the load on the base applied in the opposite direction. As in the first analysis, this simulation addresses the possibility of one of the DS train component bearing blocks binding to the rails.

2.3.2.1 Analysis Conditions

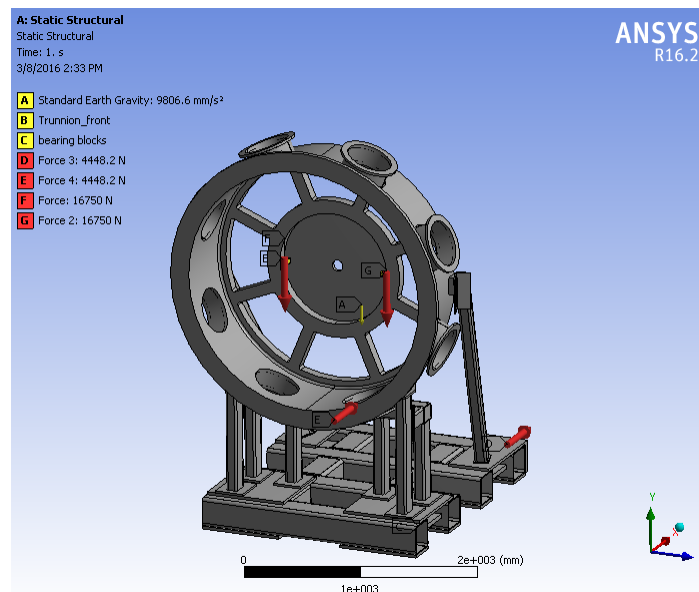


Figure 2.6: IFB analysis conditions

In the new scenario, the hydraulic cylinders will be applying the maximum load (condition D and E) in the downstream direction, notice the vector direction at the base change between Figure 2.3 and Figure 2.6. The IFB support is still responsible for gravitational load (condition A) of the IFB and muon beam stop (condition F and G). The degrees of freedom (condition B and C) shown here are the same as those simulated before.

2.3.2.2 Deformation

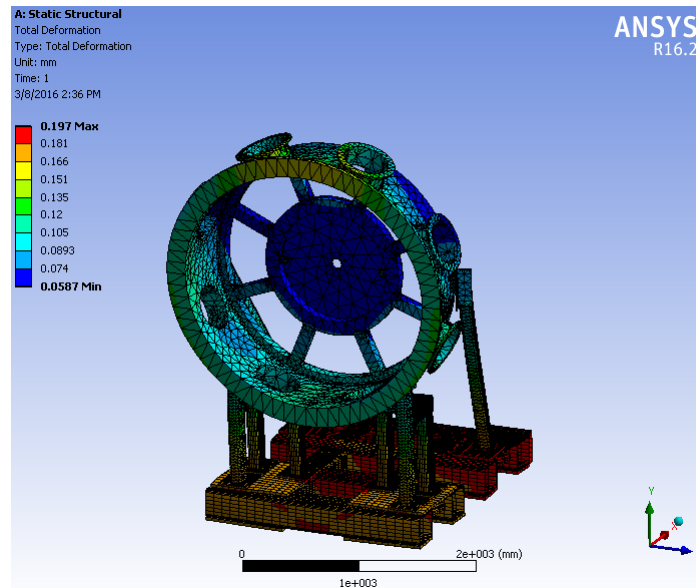


Figure 2.7: IFB extraction deformation

The deformation for the extraction process is greater than that of the insertion process, but is still relatively small and remains in the elastic range. Comparing Figures 2.4 and 2.7 it can be observed that the diagonal tube is flexing in the opposite direction, further validating the importance of the connection.

2.3.2.3 Stress

The stress that develops in this loading case is higher than that of the previous case. However, viewing Figure 2.8 there are a few local high stress regions. During the final design phase, these regions will be optimized and the weld sizes between tubing will be studied in depth. The highest stress found in this analysis is 65.6 MPa and provides a safety factor of 3.68. In this analysis the highest stress regions occur in the base where the welded members

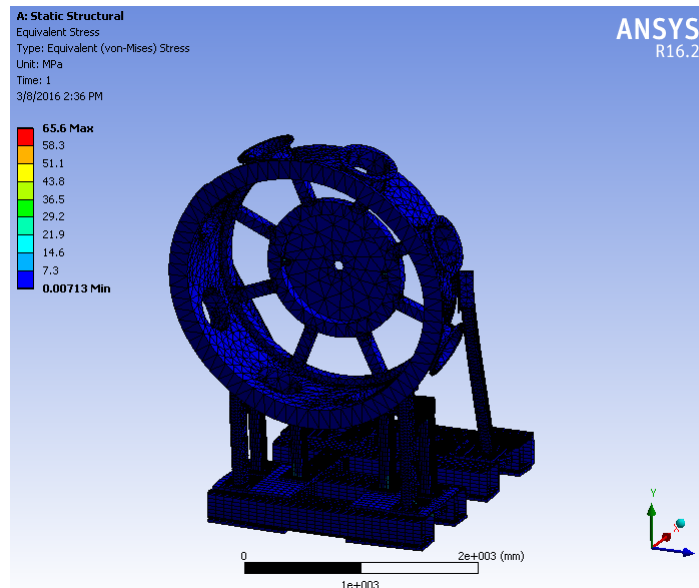


Figure 2.8: IFB extraction stress

are experiencing tension. This analysis examines the worst possible loading that the IFB and IFB support could experience.

2.3.3 Design Status Summary

At the time of this thesis submission, the IFB support is in the preliminary design iteration 2 phase with the engineering drawings currently being generated. Presently, the IFB meets the design specifications and is not expected to change much between now and the time of fabrication. Future attention will need to be given to the routing of cables that exit the DS through the ports on the IFB. Collaboration between the IFB support designer and both the electrical and concrete shielding designers is required.

CHAPTER 3

EXTERNAL STANDS

3.1 Role of the External Stands

The purpose of the 6 external stands, shown in Figure 3.1, is to provide support for the detector solenoid train while it is outside of the DS. The stands will also be used to guide the train into and out of the DS during insertion and extraction procedures. This will occur numerous times over the life of the experiment as necessary when magnetic field mapping of the DS, vacuum test cycles, alignment studies, or component servicing is required. While the train is in the DS and operation is underway, the external stands will be stored in building in the available alcoves.

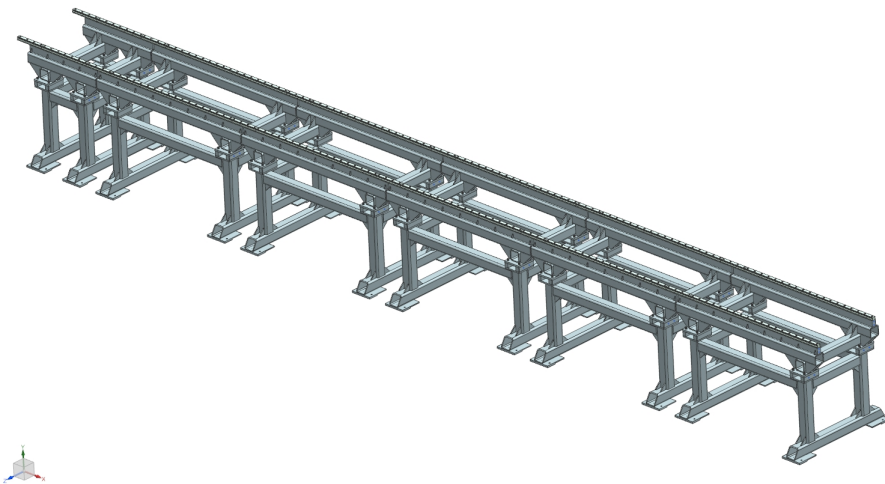


Figure 3.1: Completed iteration 2 design of the external stands

3.2 Design Specifications

The design of the external stands must satisfy several different criteria. To test the alignment procedure of the external stands, a prototype (the current design) of the upper weldment of the shortest stand was ordered, see drawing number F10040614 in the Appendix. Upon arrival at Fermilab, it was installed on one end of A “mock up” rail system and measured, the details will be discussed in a later section.

3.2.1 Geometric and Spacial Requirements

The need for having external stands is to bridge the gap between the floor and the rails inside of the DS. Considerations have been made to ensure that appropriate gaps are left between stands. Additionally, designing the stands in such a way that the legs will rest on steel tracks embedded into the concrete floor was done. Special rail links have been designed that connect the stands together and form a continuous rail. One unique feature that has been included in the design is that they are vertically adjustable. The external stands have been separated into two weldments that bolt together. A slot has been added to the lower portion of the stand that allows room for a jack to be placed. To achieve the proper height, the upper weldment will be jacked up and, shims will be added to the contact interface. After this, the upper weldment will be lowered and securely tightened. This process will be discussed in detail in section 3.5.

3.2.2 Magnetic Requirements

One of the critical studies that will be conducted prior to experiment operation is the magnetic field mapping of the detector solenoid. At the time this is being done, the external stands will be supporting the DS train, and cannot be removed from their nominal position. If the stands were made of a ferromagnetic material such as AISI 1020 steel, the magnetic field lines near the downstream end of the DS would be distorted. This would have a negative impact on the final interpretation of data. For this reason, the stands have been made of 6061-T6 aluminum which is non-magnetic. The temper on the aluminum significantly increases the yield strength to 214 MPa making it a good choice for this structural application [13].

3.2.3 Structural Requirements

An important aspect of the external stand design is the justification of the structural strength. This will be achieved by performing an analytical analysis of the stress, internal moments, and deflections under the maximum loading conditions. These results are also to be confirmed through an ANSYS finite element analysis. The desired project design safety factor to be achieved for the external stands is 2, and is higher than the design safety factor of 1.65 found in the Aluminum Design Manual: 2010.

3.3 Analytical Analysis

To analyze the system the top of the rails will be approximated as a simply supported beam, see Figure 3.2. While the actual system will be a bolted connection, it is common

practice in engineering to make conservative assumptions when doing hand calculations. This assumption will yield a higher deflection and lead to a larger safety factor for the design. An additional assumption that is made for this analysis is that the length of the beam is 1800 mm, while the actual stand will be 2500 mm. The distance between the center of the supports for this beam is 1800 mm and is the reason that is was the length used for this study.

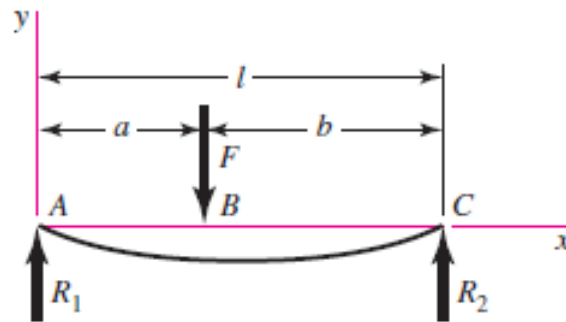


Figure 3.2: Loading schematic [14]

3.3.1 Maximum Deflection Loading Parameters

The maximum loading condition occurs when the sum of the loads can be replaced by a single equivalent load at the center of the support structure. This will produce the maximum possible internal moment causing the largest possible deflection.

The loads that cause the largest loading occur from the calorimeter and MBS (shown as $m_1 \rightarrow m_4$ in Equation 3.2 and 3.3) [11]. The distance between loads is fixed, but at a specific location on the stands they cause the largest possible moment. Setting the moment produced by a centered load with mass (m), gravity (g), and distance ($L/2$) equal to the mass ($m_1 \rightarrow m_4$) of the MBS and calorimeter, gravity (g), and variable position ($f(x)$) the location can be determined.

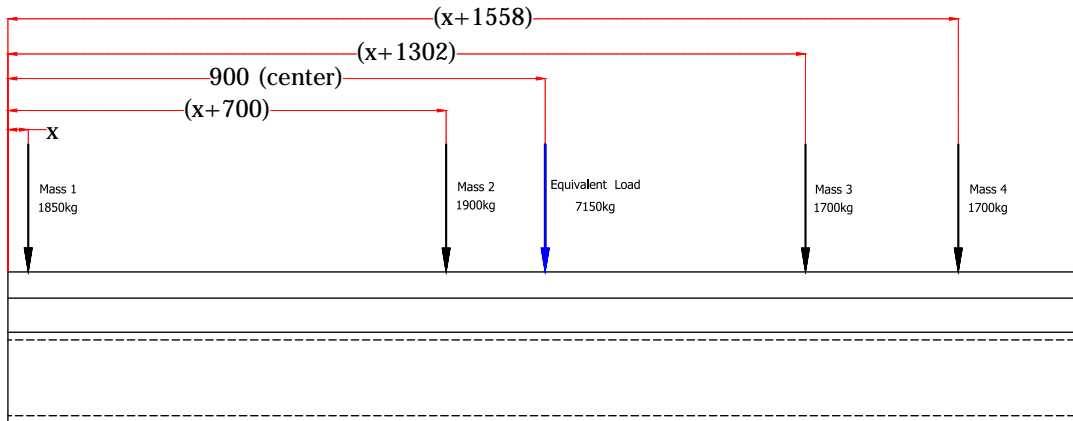


Figure 3.3: Calorimeter load (left two black arrows), MBS load (right two black arrows) centered load (blue)

$$M_{eq} = \sum mg \frac{L}{2} = \sum mf(x)g \quad (3.1)$$

$$\begin{aligned} \sum mg \frac{L}{2} &= (m_1 + m_2 + m_3 + m_4)g \frac{L}{2} \\ &= (1850\text{kg} + 1900\text{kg} + 1700\text{kg} + 1700\text{kg}) \left(9.81 \frac{\text{m}}{\text{s}^2}\right) \frac{1.8\text{m}}{2} \end{aligned} \quad (3.2)$$

$$\begin{aligned}
\Sigma mgf(x) &= [(m_1)(x) + (m_2)(x + 700\text{mm}) + (m_3)(x + 1302\text{mm}) + \\
&\quad (m_4)(x + 1558\text{mm})]g \\
&= [(1850\text{kg})(x) + (1900\text{kg})(x + 700\text{mm}) + (1700\text{kg})(x + 1302\text{mm}) + \\
&\quad (1700\text{kg})(x + 1558\text{mm})]g
\end{aligned} \tag{3.3}$$

Setting $\Sigma mg\frac{L}{2}$ equal to $\Sigma mf(x)g$ and using a mathematical solver yields the result: $x = 34.0\text{mm}$.

3.3.2 Centroid Calculations

In order to determine the moment of inertia of the system, the centroid must first be found. It's important to note that the centroid in this configuration is not the center of gravity since two different materials are used in the beam. So that symmetry can be utilized, the y-axis (vertical) has been defined to be in the center of the beam. The z-axis (horizontal) has been defined to at the bottom of the beam, parallel with the square tubing bottom surface. The first step in determining the neutral axis of the composite beam is to determine the centroids of each individual material component. Once this is completed the neutral axis of the system can be determined.

3.3.2.1 Aluminum Centroid

The 6061-T6 aluminum portion of this beam is comprised of the 6 x 6 (inch) square tube and the 2.5 x 3.0 (inch) platform bar and is modeled as a one part for this analysis. This

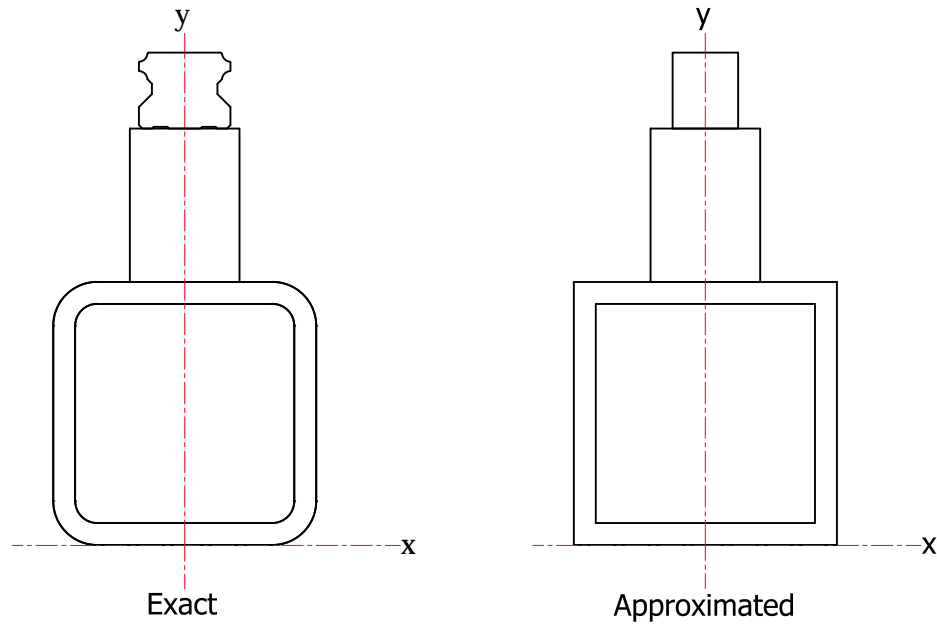


Figure 3.4: Beam cross-sectional view

assumption is made since the platform bar and square tube are welded together. Using the composite method the centroid of the aluminum components is calculated.

Table 3.1: Aluminum centroid calculations

Component	W (mm)	H (mm)	A (mm ²)	\bar{y} (mm)	$\bar{y}A$ (mm ³)
Square Tube	152.4	152.4	23226	76.2	1769800
Sq. Tube Hollow Area	127.0	127.0	-16129	76.2	-1229000
External Stand Bar	60.0	88.9	5334	196.85	1050000
Totals	-	-	12431	-	1590800

$$\bar{y}_{al} = \frac{\Sigma \bar{y}A}{\Sigma A} = \frac{1590798\text{mm}^3}{12431\text{mm}^2} = 128.0\text{mm} \quad (3.4)$$

3.3.2.2 HPM75 and Standard Steel Rail Centroid Calculations

The steel portion of this structure is the THK HSR55 rails. As can be seen in Figure 3.4, the shape of the rails is complex. To simplify the calculations the area is assumed to be rectangular with the dimensions 38 mm (the narrowest width) by 44 mm (the overall height). Thus the centroid located at half of it's height:

$$\bar{y}_{st} = 241.3\text{mm} + \frac{44\text{mm}}{2} = 263.3\text{mm} \quad (3.5)$$

3.3.2.3 Neutral Axis Calculations

In the case of a non-homogeneous beam, the area moments of inertia are calculated about the neutral axis (the location where the stress and strain is zero). The neutral axis has been denoted as x' (horizontal) and y' (vertical) and being centered at the composite centroid, see Figure 3.5. The following equation is used to determined the exact location of this axis, with E representing the modulus of elasticity, \bar{y} the centroid for each material, and A the cross-sectional area.

$$E_{st}\bar{y}'_{st}A_{st} + E_{al}\bar{y}'_{al}A_{al} = 0 \quad (3.6)$$

To determine the location of the neutral axis, the constants c_1 and c_2 have been defined to be the vertical distance from the $y' = 0$ (neutral) axis to the top and bottom of the beam, respectively. Through algebraic manipulation the following equation has been formed and solved.

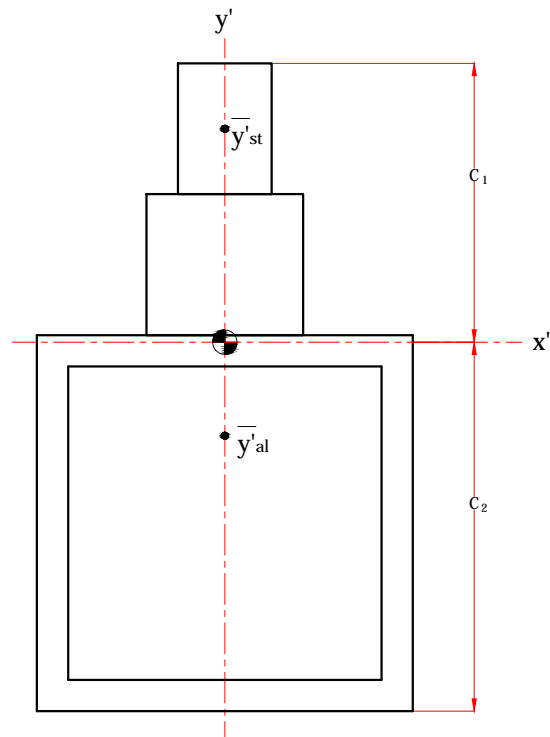


Figure 3.5: Moment of inertia for steel, aluminium, and combined

$$(193\text{GPa})(c_1 - 22.0\text{mm})(1672\text{mm}^2) + (69.6\text{GPa})(c_1 - 157.3\text{mm})(12431\text{mm}^2) = 0 \quad (3.7)$$

$$c_1 = 120.5\text{mm} \text{ and } c_2 = 164.8\text{mm} \quad (3.8)$$

3.3.3 Area Moment of Inertia and Weighted Flexural Rigidity

Calculations

To determine the deflection about the neutral axis, the area moment of inertia (I) must be calculated. Using the parallel-axis theorem, this value can be found by summing local the area moment of inertia from the materials centroid (I_{xx}) and the total area (A) multiplied by the distance (d) from the local area moment of inertia to the neutral axis.

$$\begin{aligned}
 I_{st} &= I_{xx} + A_{st}d_{st}^2 \\
 &= \frac{bh^3}{12} + A_{st}(\bar{y}_{st} - c_2)^2 \\
 &= 1.6492\text{E}7 \text{ mm}^4
 \end{aligned} \tag{3.9}$$

The same method is applied to the aluminum section utilizing the values from Table 3.3.3.

Table 3.2: Area moment of inertia calculations

Component	Base (mm)	Height (mm)	A (mm ²)	\bar{y} (mm)	d (mm)
6" x 6" Sq. Tube	152.4	152.4	23226	76.2	88.6
Tube Hollow Area	127.0	127.0	-16129	76.2	88.6
External Stand Bar	60.0	88.9	5334	196.85	32.05

$$\begin{aligned}
 I_{al} &= \Sigma(I_{xx} + Ad_{al}^2) \\
 &= \Sigma\left(\frac{bh^3}{12} + A_{al}d_{al}^2\right) \\
 &= 3.9677\text{E}8 \text{ mm}^4
 \end{aligned} \tag{3.10}$$

Since this beam is bimetallic the weighted flexural rigidity is calculated using the elastic modulus (E) and the area moment of inertia (I) for both materials.

$$\begin{aligned}\overline{EI} &= (E_{st}I_{st} + E_{al}I_{al}) \\ &= 9.306\text{E}12 \text{ N-mm}^2\end{aligned}\tag{3.11}$$

3.3.4 Deflection

One of the critical concerns regarding the installation and extraction of the detector solenoid train is that it be able to roll into and out of the bore as smoothly as possible. To facilitate this, minimal rail deflection is desired. Following the THK guideline for *error allowance in vertical level between rails*, the deflection (δ) should follow the manufacturer guideline: $\delta \leq 600\mu\text{m}/\text{m}$ length of rail [15]. To determine the deflection throughout the beam the principle of superposition will be applied.

Superposition resolves that the effect of combined loading on a structure can be determined by finding the effect of each load separately and then adding the results together algebraically. For superposition to be applied the following conditions must be met:

1. Each effect is linearly related to the load that produces it.
2. A load does not create a condition that affects the result of another load.
3. The deformations resulting from any specific load are not large enough to appreciably alter the geometric relations of the parts of the structural system. (Budynas, Nisbett, and Shigley, 2011, p. 153)

The equations for the for the deflection at each point are as follows with the variables corresponding to Figure 3.2 [14].

$$\Sigma y_{ab} = \frac{Fbx}{6EI} [x^2 + b^2 - l^2] \quad (3.12)$$

$$\Sigma y_{bc} = \frac{Fa(l-x)}{6EI} [x^2 + a^2 - 2lx] \quad (3.13)$$

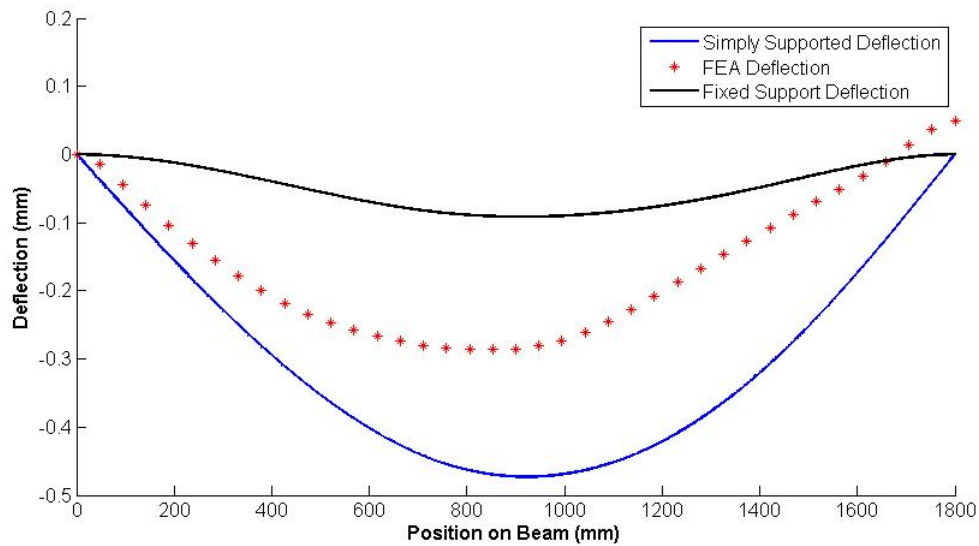


Figure 3.6: Theoretical deflections compared to FEA

Summing the deflections from the individual loads yields a higher deflection when compared to FEA result, which uses the actual geometry. This is due to the fact that the beam is not truly simply supported, and contains gussets which increase the beams stiffness. However, the beam does not exactly follow distribution given by a fixed support plot either. In reality the beam deflection falls in the region between fixed and simply support, which is what one could expect from a real beam. Figure 3.6 does verify that using a simply supported beam is a conservative assumption and will lead to higher stresses than those experienced by the stand. Viewing the deflection from the FEA is can be seen that the deflection is not symmetric like it is for the analytical solutions. This develops since one of the loads falls on

top of the beam where a gusset has been added. This causes the deflection due to that load to be minimized.

3.3.5 Stress

To determine the maximum bending stress in the beam the moment at that point must be calculated. The equation for the internal moment of a beam follows the governing equation:

$$M = EI \frac{dy^2}{dx^2} \quad (3.14)$$

Applying this equation yields the internal moment distribution seen in Figure 3.7. Note that the slope of the moment changes at the points where the loads are applied. The maximum moment is found and will be utilized in determining the stresses in the bimetallic beam.

$$\begin{aligned} \sigma_{st} &= \frac{-ME_{st}y}{EI} \\ &= \frac{-ME_{st}c_1}{EI} \\ &= 32.6\text{MPa (Compression)} \end{aligned} \quad (3.15)$$

$$\begin{aligned} \sigma_{al} &= \frac{-ME_{st}y}{EI} \\ &= \frac{-ME_{st}c_2}{EI} \\ &= 16.1\text{MPa (Tension)} \end{aligned} \quad (3.16)$$

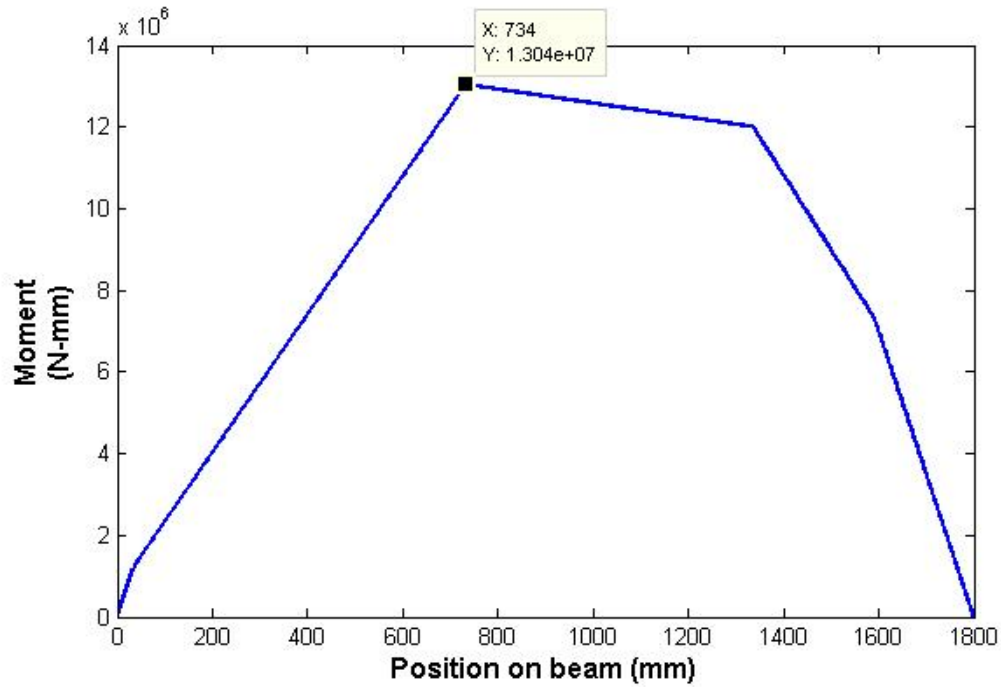


Figure 3.7: Theoretical internal moment for the external stands

Another important aspect to consider in the design of a beam is that the end supports can withstand the necessary reaction forces. To determine reaction forces on each end of the beam, the following equations and variables from Figure 3.2 are used.

$$\begin{aligned}
 R_1 &= \Sigma \frac{Fb}{l} \\
 &= 35070\text{N}
 \end{aligned}
 \tag{3.17}$$

$$\begin{aligned}
 R_2 &= \Sigma \frac{Fa}{l} \\
 &= 35070\text{N}
 \end{aligned}
 \tag{3.18}$$

The smallest cross-sectional area on the vertical support is the square tubing, so it is important to calculate the compressive stress in the member. Using the reaction force (F) and area (A) found in Table 3.3.3 the compressive stress is determined.

$$\begin{aligned}
 \sigma_c &= \frac{F}{A} \\
 &= \frac{35070\text{N}}{(23226 - 16129)\text{mm}^2} \\
 &= 4.94\text{MPa}
 \end{aligned}
 \tag{3.19}$$

The stresses found in Equations 3.15, 3.16, and 3.19 result in a minimum safety factor of 7.6 with respect to the yield strength of the materials. Next the stress throughout the entire stand will be considered.

3.4 Finite Element Analysis

To determine the stress, safety factor, and deflection an ANSYS finite element analysis was performed. As shown in the analytical analysis, the maximum loading conditions are used. While adhering to a safety factor of 2 was an important part of the design, the most challenging part of the design optimization was reducing the deflection to the acceptable level.

3.4.1 Loading Conditions

In the analytical analysis point loads were used for simplicity. However, this analysis will use the actual distributed loading areas (condition C-J). Standard earth gravity (condition

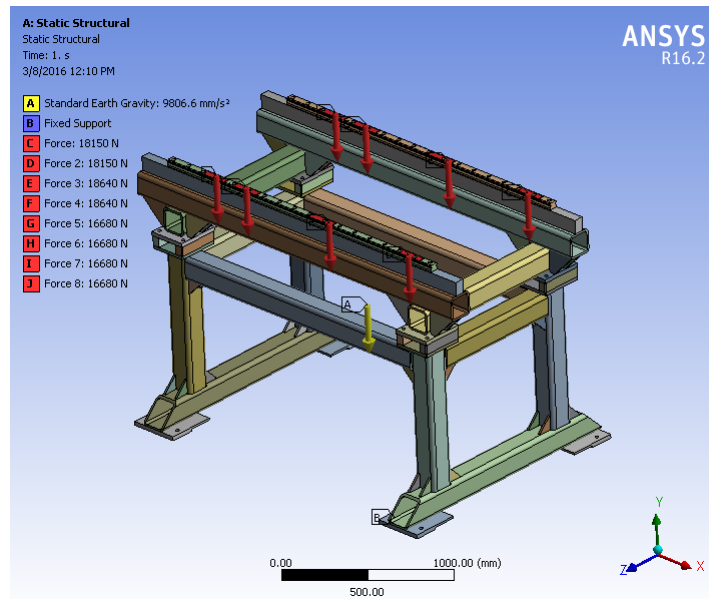


Figure 3.8: External stand loads from tracker, calorimeter, and gravity

A) is also applied in this model, which takes into account the stands weight. Since the stands will be bolted into the floor plates the bottom of each “foot” has been constrained in all directions (condition B).

3.4.2 Total Deformation

The total deformation of the stand are given as magnitude. The red shading is the highest deflection and occurs at the midpoint of the beam. The blue is the least deflection which occurs on the feet near the ends. Comparing the maximum total deflection to the maximum vertical deflection yields almost the same amount. However certain regions will have some component of x and z deformation.

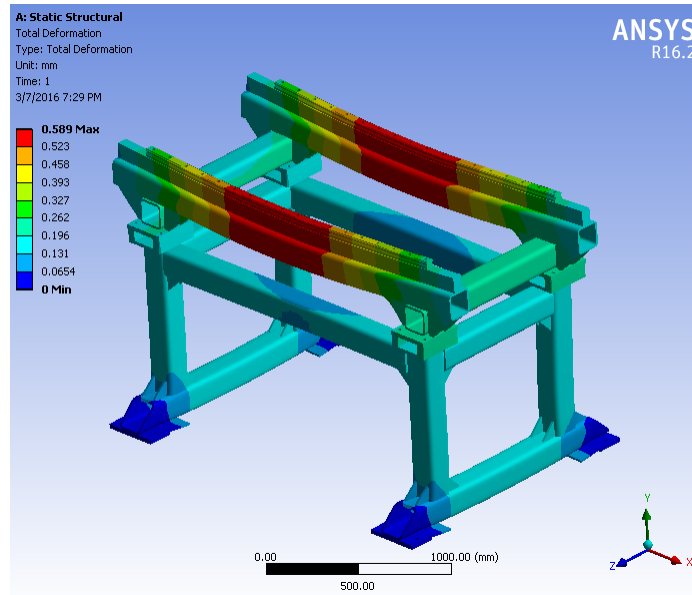


Figure 3.9: External stands total deformation

3.4.3 Vertical Deformation

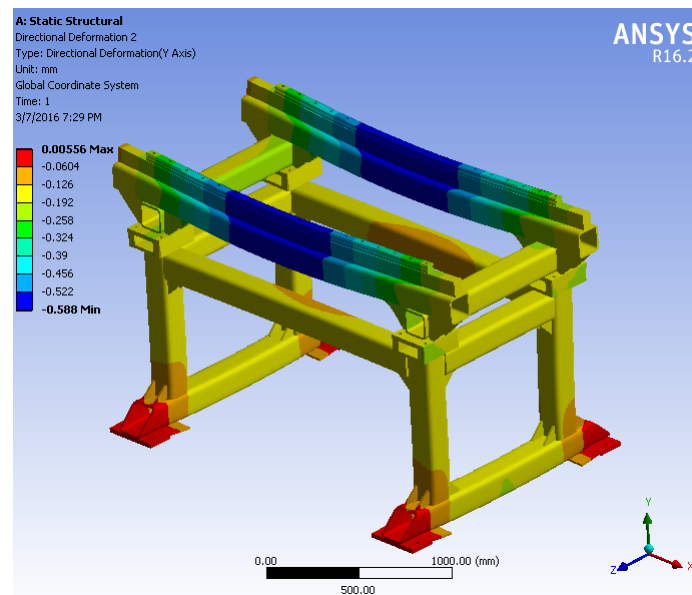


Figure 3.10: External stand vertical deformation

The maximum vertical displacement of the rails is $588 \mu m$ in the downward direction. The criteria for the design is that it should not exceed $600 \mu m$ per 1 meter of travel. Half the length of this stand is 1.25 meters, thus the stand is within the allowable deflection range.

3.4.4 Stress

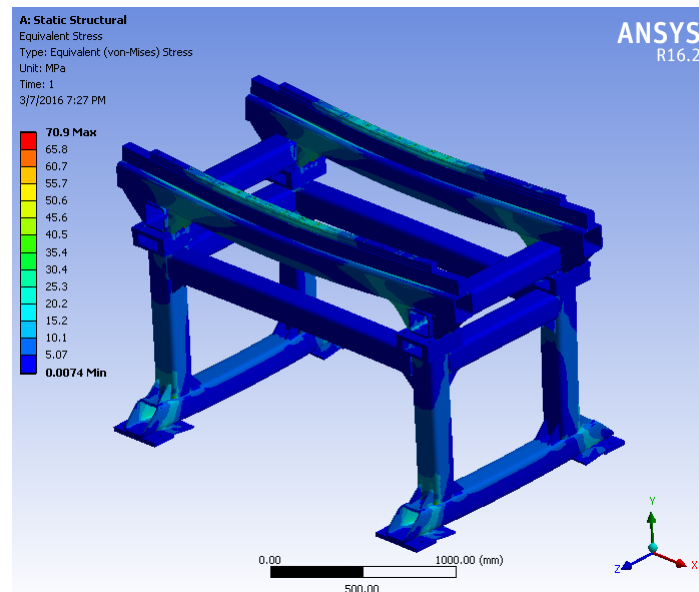


Figure 3.11: External stand von-mises stress

Analyzing the stress of the external stand was a challenging endeavor. As it appears from Figure 3.11 the visible stresses do not exceed 52.5 MPa. However taking a very close look at some of the connections, stresses near 71 MPa are reached. The areas that these high stress points occur are places where sharp corners meet flat, bending surfaces. In finite element terms this is called a considered singularity. In reality all physical surfaces will have some radius and the stress in such areas will not be so high. Furthermore, the extra material that will be added to these areas by welding has not been included in this model.

An additional stress concern in this design is that weld affected areas have a lower yield strength than the nominal strength of the tempered aluminum. When welding occurs in an area the region within 25.4 mm (1 inch) of the weld center-line is considered to be "weld-affected". The strength of the material in these zones depends on the base metal, temper, and the alloy filler used for the weld. For 6061-T6 aluminum that has been welded with 5183, 5356 or 5556 alloy filler the yield strength is 105 MPa. [13]

3.4.5 Safety Factor

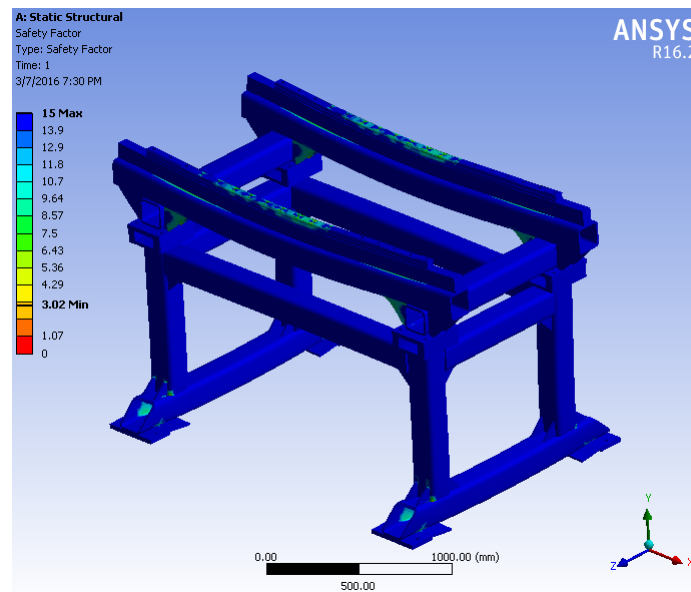


Figure 3.12: External stand safety factor

Even with several small stress singularities, the safety factor of this design is above 3 relative to the strength of the tempered aluminum. As discussed in the stress section, the regions that are weld-affected will have a lower yield strength and must be reviewed during the final phase of the design.

3.5 Mock Up Testing

As shown in Figure 1.8, a system of external stands will be used to support the interior DS components and transport them into the DS bore. In order to be sure that the desired alignment between stands could be achieved the top weldment of the small stand was fabricated. This system was tested on a rail mock up at Fermilab in the Industrial Center Building between February 15th and 24th, 2016 and shown in Figure 3.13. Four small weldments were used to imitate the bottom portion of the external stands.

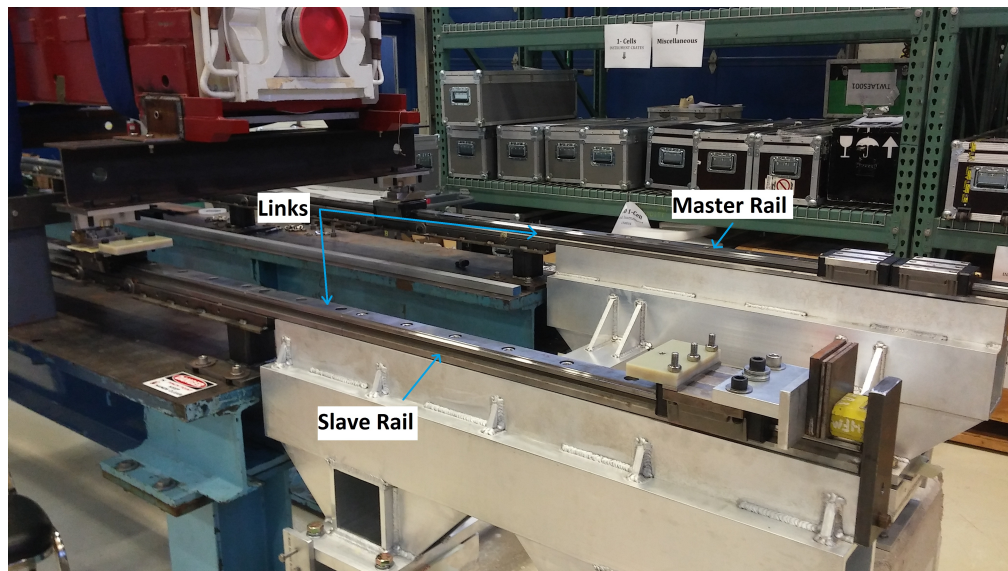


Figure 3.13: External stand mock up

By design, the two surfaces of the top segment to which the rails are bolted is machined as a plane which has a maximum out-of-flatness tolerance of $75 \mu m$. The top segment can then be leveled as a whole by four inclined-plane jacks that fit in a slot between the upper and lower weldment, see Figure 3.14. The procedure developed for this test will be replicated in the actual Mu2e experiment.



Figure 3.14: External stand adjustment region

3.5.0.1 Adjustment Methodology

1. Inspect the upper stand weldment to ensure that the platforms to which the rails will be attached are flat within $75 \mu m$.
2. Bolt the four lower supports into the upper segment.
3. Bolt the main (center) rail segments onto the upper stands.
4. Align the assembly into its approximate desired position, both vertically and laterally, using a straightedge.
5. Bolt the links into place, aligning them laterally with the original rail with a straight edge.
6. The alignment crew takes measurements of the original rails which comprise the already-constructed mockup. Vertical measurements are taken of both rails and lateral measurements are taken of the master rail only. An ideal plane is created from the measurements, which represents a best-fit extension of the original rails.

7. Adjust the upper external stand to the ideal frame.
 - (a) Place the inclined plane jacks into the four appropriate openings between the bottom stands and the top segment.
 - (b) Loosen the bolts which attach the upper segment to the lower stands.
 - (c) Raise or lower the upper stand to the vertical positions defined by the ideal frame, from instructions given by the alignment crew.
 - (d) Place shims between upper and lower stands to fill in the spaces between them.
 - (e) Adjust the stand laterally in both x and z using adjustment angles.
 - (f) Tighten the bolts to firmly attach the upper and lower stands.
 - (g) Measure the vertical and lateral positions of the rails.
 - (h) Add or subtract shims or adjust laterally to correct any positional errors.
 - (i) Repeat steps e-h until stand is within $125 \mu m$ of the ideal frame.
 - (j) Slightly loosen the bolts which attach the slave rail to the upper external stand segment.
 - (k) Using the alignment cart adjust the lateral position of the slave rail, including the link.
 - (l) Loosen the bolts slightly on the master-side link.
 - (m) Using the alignment cart, adjust the lateral position of the master link.
8. Take a final measurement of both the master and slave rails, laterally and vertically.
9. Roll the heavy weight (4200 kg) conventional Main Injector quadrupole over the external stand to test the ease of travel.
10. Roll the heavy weight off the external stand.

11. Measure the external rails after the magnet has been removed.
12. Review the results to ensure desired tolerances were achieved.

3.5.0.2 Adjustment Results

The measurements from before and after loading can be seen in Figure 3.15, where the deflection relative to the initial alignment is observed. During loading both sides temporarily deflected by $75\ \mu\text{m}$ near the center of the support. When comparing the results, from before and after loading, small variations were expected since layers of shims can be slightly compressed or flattened. However, the objective of this experiment was to ensure rails stay stay within $125\ \mu\text{m}$ of the original plane. Based upon the measurements, shown in Figure 3.15, the alignment stayed within tolerance. From this experiment, it was concluded that the desired alignment can be achieved when the stands are fabricated and aligned in the detector hall.

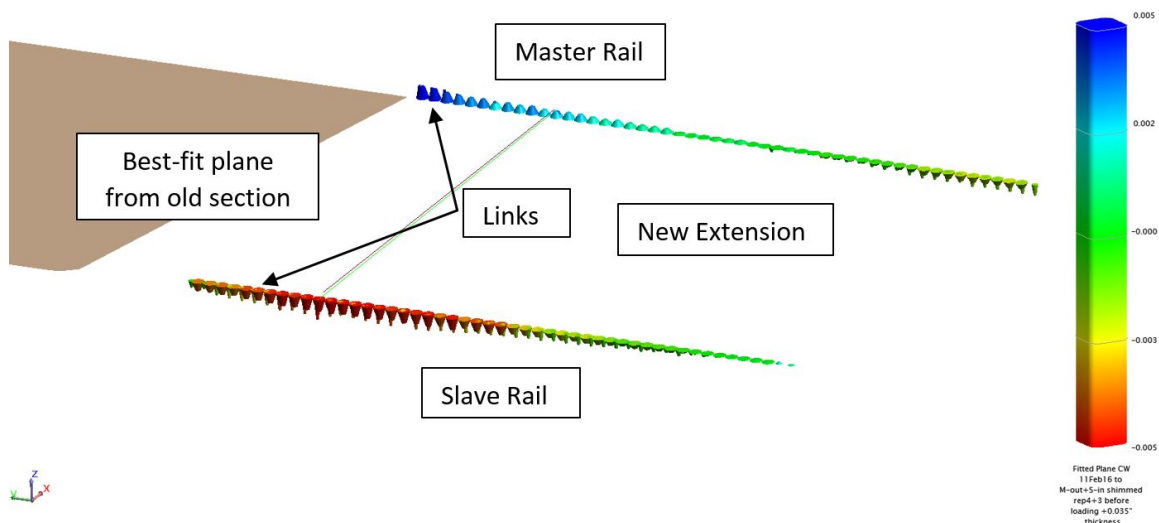


Figure 3.15: External stand measurements large cones (before loading), small cones (after loading)

3.6 Design Status Summary

At the time of this thesis submission, the external stands are in the preliminary design iteration two phase. It is expected that only small changes will be made (if any) during the final design phase. Detailed drawings of the external stands can be found in the Appendix. One of the primary aspects to consider during the next phase is the final height difference between the floor and the center of the DS. Until the concrete floor has been poured and measured, the final dimensions cannot be determined. Fortunately, all of the custom adjustments can be made in the overall leg height and then smaller shimming can be performed at the stand mount.

CHAPTER 4

DETECTOR SOLENOID THERMAL CONTROL

4.1 Purpose of a Thermal Management System

As discussed in section 1.3.3, the DS contains a cold mass (cooled to 5K) between two concentric cylinders. The inner cylinder is a warm bore and provides a location and environment to acquire data. There are two motivating factors in controlling the temperature of the DS warm bore. The first is that if the temperature is allowed to drop below 0 the bore, and when the DS is brought back to atmospheric pressure (from high vacuum) the water vapor in the air will condense on the cold surfaces. This is problematic since numerous electronic circuit boards, sensors, and wires exist inside the DS. The effects of condensed water on these components would cause failure. The second area of concern is the thermal contraction that would be experienced by the rails system and consequently the DS train. Thermal contraction could cause two potential problems: binding of the rails and misalignment of components. To achieve optimum performance, the parallelism between rails should be within $70 \mu m$ [15]. In addition, the desired positional accuracy of the DS train components is ± 2 mm and in some cases ± 1 mm. This accuracy allows a specific spectrum focus for the physics measurements. If a large temperature gradient developed, then it would be difficult to achieve this tolerance. To determine if there was a need for temperature control, a detailed deflection and stress analysis of the detector solenoid under vacuum was completed.

4.2 Heat Transfer

Since the tube boundary conditions and geometry are symmetric both axially and tangentially, the problem can be analyzed in 2D. The 2D model is a quarter cross-sectional cut. The simplified model of the DS is represented in Figure 4.1. The two ends of the solenoids and the outside are at 20°C and the radiation heat transfer from the 293.15K (20°C) vessel to the 80K MLI is represented by a heat flux $q'' = 1.5 \frac{W}{m^2}$. This value was determined by measurements from Fermilab engineers in prior experiments and is the value assumed for design purposes [16].

Conduction heat transfer occurs inside the material and is expressed by the Fourier law, Equation 4.1.

$$\dot{Q}_{cond} = -kA \frac{\partial T}{\partial z} \quad (4.1)$$

With \dot{Q}_{cond} representing the heat transfer rate, A the cross-sectional area, and $\frac{\partial T}{\partial z}$ the change in temperature with respect to the Z direction. The coefficient of thermal conductivity for 316L stainless steel ranges between $14 \frac{W}{mK}$ and $15.9 \frac{W}{mK}$, and is assumed to be $k = 14.6 \frac{W}{mK}$ in this analysis.

With reference to Figure 4.1, the geometry of the detector solenoid is defined in Table 4.1

Table 4.1: DS geometry

Inner Shell ID [mm]	Inner Shell tk [mm]	Outer Shell OD [mm]	Outer Shell tk [mm]	End Wall tk [mm]	Length [mm]
1900	20	2656	20	40	10900

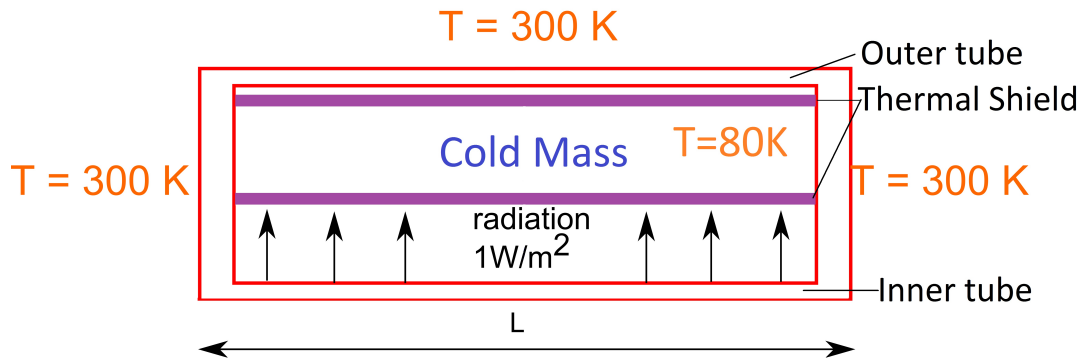


Figure 4.1: Simplified scheme of the solenoid and vessel.

4.2.1 Preliminary DS Finite Element Analysis

Once of the first steps in many engineering analyses is to perform a simplified analysis to develop an understanding of the physics of the system. This was done by for the DS by assuming a 2D model and applying boundary conditions.

4.2.1.1 Boundary Conditions

The temperature of the air surround the DS will be controlled to be between $20\text{-}27\text{ }^\circ\text{C}$. To be conservative the end of the DS is assumed to be equal to the lowest possible air temperature. To justify this is a valid assumption, hand calculations were performed by Fermilab engineers that showed the convection environment caused air and ends of the DS to remain the same temperature within one degree [16]. The expected radiative heat flux of $1.5\text{ } \frac{\text{W}}{\text{m}^2}$ is applied to the outer diameter of the inner (warm) bore. Within the 3000 element

model a symmetry plane has been imposed on the right side, where the center of the DS would be located.

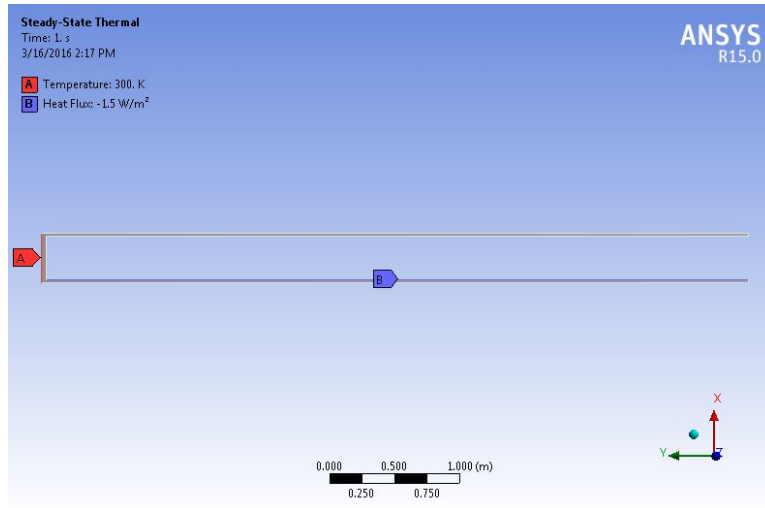


Figure 4.2: Boundary conditions and load in vacuum with symmetry imposed

4.2.1.2 Temperature Distribution

The temperature different between end and center of the DS in analysis was found to be 75°C. This shows a very significant temperature change that required a more in depth study.

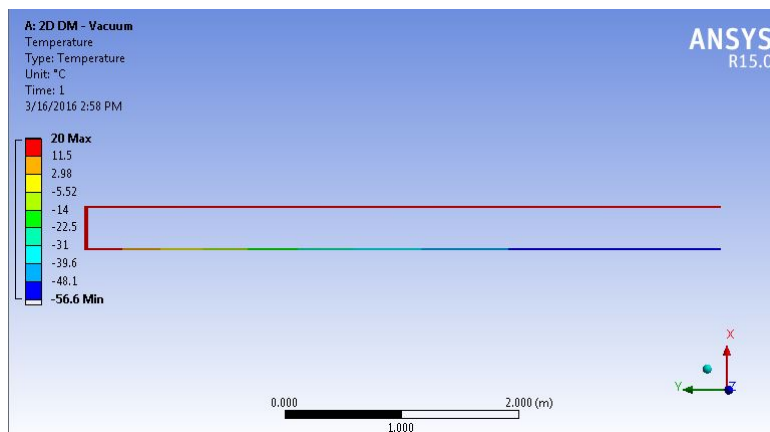


Figure 4.3: Temperature distribution in half of the model of the DS

4.2.2 Secondary DS Finite Element Analysis

After completing the simplified 2D case and reviewing the results, it became clear that the full model should be constructed. The ultimate concern with a large thermal gradient is that high deflection and stresses will develop in the system. To analyze these properties a coupled steady-state thermal and static structural analysis has been performed.

4.2.2.1 Thermal Boundary Conditions

The applied boundary conditions in the steady-state thermal analysis are the same as those imposed in the 2D case. A key difference that has been added to this model is the addition of the “box dimensions” of the internal rail geometry.

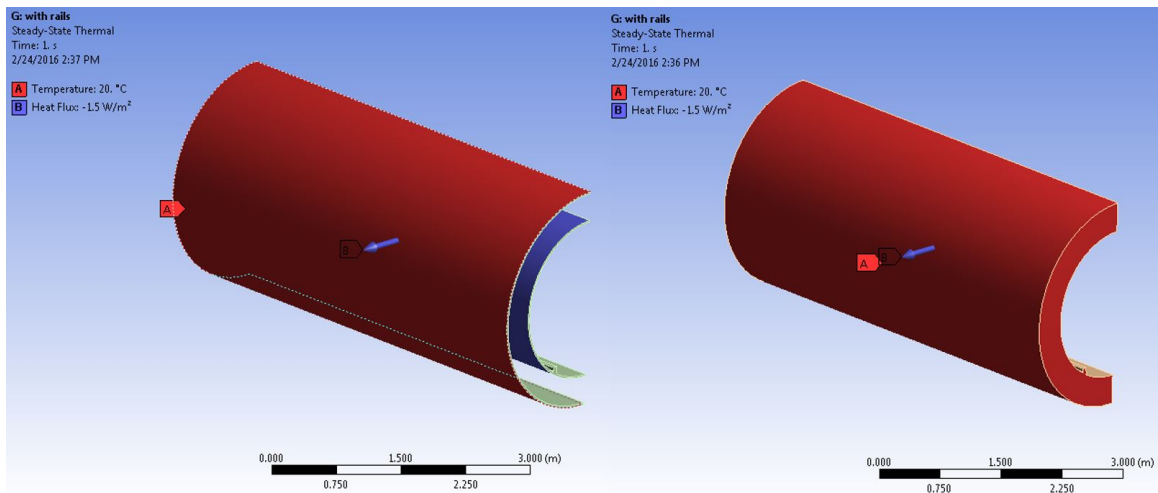


Figure 4.4: Boundary conditions and load in vacuum

4.2.2.2 Temperature Distribution

Completing the analysis results in a temperature that ranges from 20°C on the ends and reaches -50°C at the center, see Figure 4.5. This change is similar to that observed in the 2D analysis. To determine the impact this has on the structural integrity of the DS, the temperature data was imported in an ANSYS static structural environment.

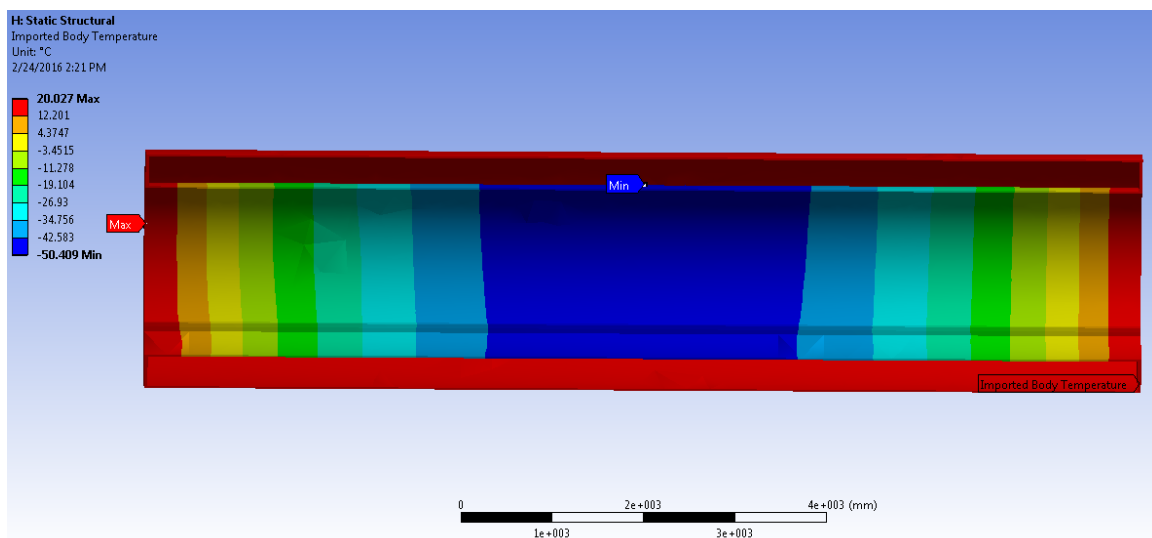


Figure 4.5: Steady state temperature distribution

4.2.2.3 Structural Boundary Conditions

Once the temperature profile was added to the model, the outside diameter of the outer shell was set constrained to have zero displacement (fixed). In reality the DS will have two stiffening rings that surround it as well as saddle supports that extend to the floor. While this assumption may lead to higher stress near the constraint, the overall deflections will be smaller (more conservative) than those that will actually develop.

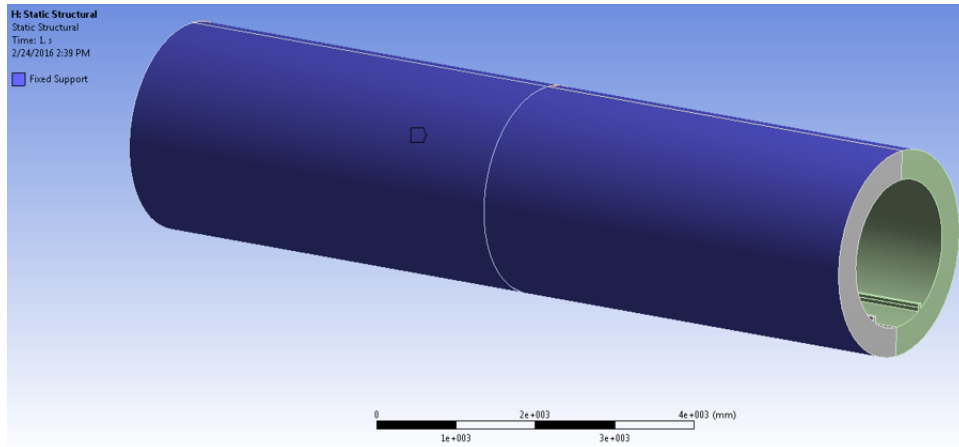


Figure 4.6: Boundary condition: displacement constraints

4.2.2.4 Deformation

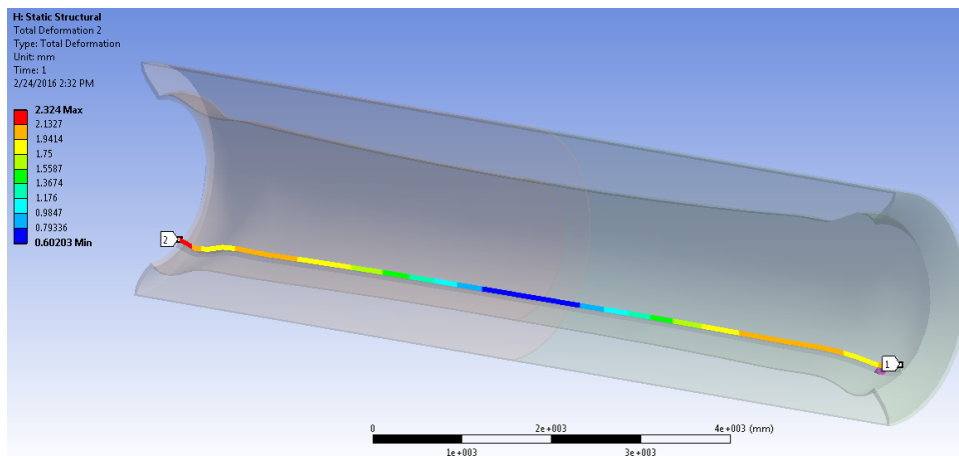


Figure 4.7: Total deformation from thermal contraction

Since the region of interest in this study is the rail deflection, the nodes along the rail were mapped to a path so that the the deformations could be examined. Reviewing the magnitude of the total deformation is can be seen that the deformation exceeds what is allowed for the system. To obtain a better understand of the deformation components the deflection in each direction will be reviewed.

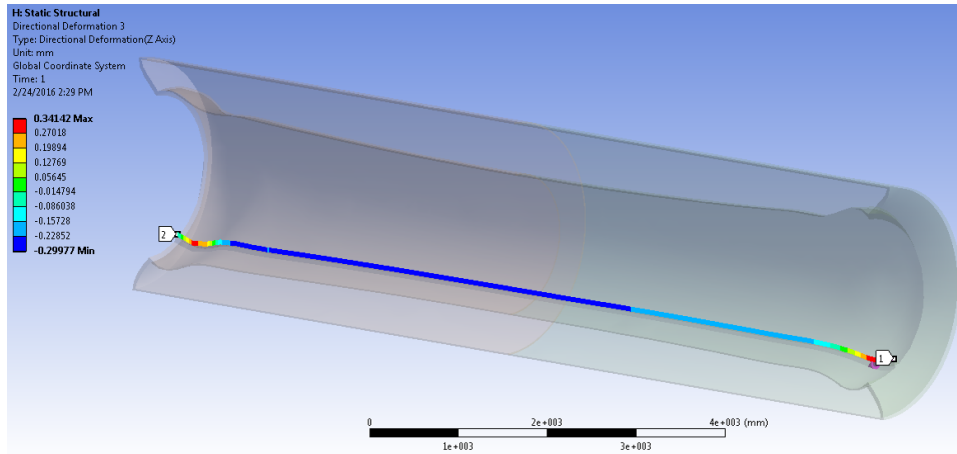


Figure 4.8: Transverse deformation from thermal contraction

Figure 4.8 shows that the maximum transverse displacement is 0.34 mm. The rails in the DS will be installed to have a nominal separation of 1000 mm between the center of the rails. The components on the master rail side will remain in a fixed position while the slave side can float (discussed in section 1.3.3.1). Considering this the center of the detector component would shift away from or towards the slave side at twice the magnitude shown in Figure 4.8.

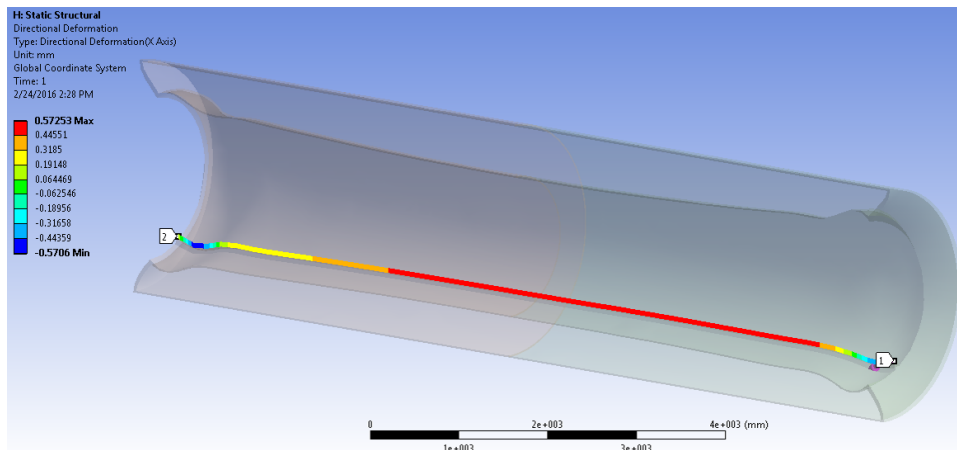


Figure 4.9: Vertical deformation from thermal contraction

The vertical displacement in the DS is symmetric between the master and slave side. As can be expected, this magnitude is greatest at the center of the DS where the temperature change is greatest shown in Figure 4.9.

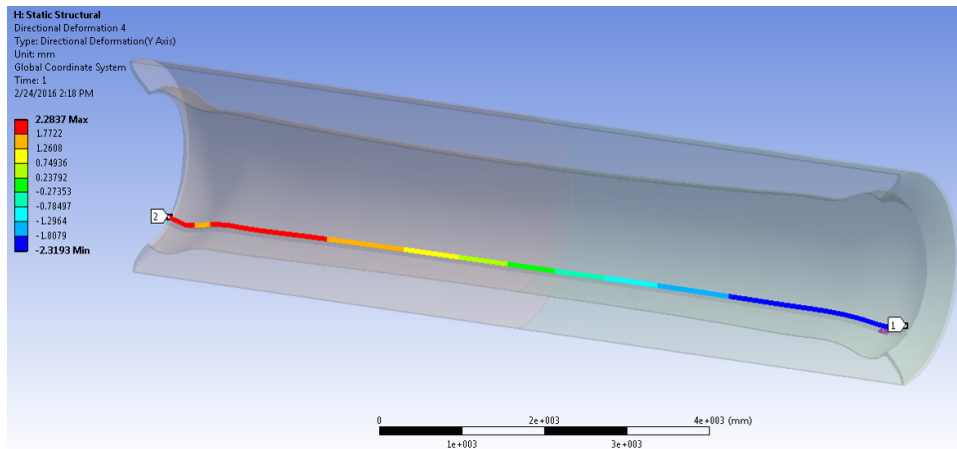


Figure 4.10: Axial deformation from thermal contraction

The axial displacement is the most significant contributor to the overall deflection. This can be explained through Equation 4.2, where L is the length, α is the coefficient of thermal expansion, and T is the temperature.

$$\Delta L = \alpha L \Delta T \quad (4.2)$$

From this governing equation it can be seen that by increasing the length, the change in length (ΔL) linearly increases. Since the tube is longest in the axial direction, this is the direction of maximum displacement. It is important to note that while the rails and DS will shrink, the position of the DS train will be fixed relative to the downstream end IFB to VPSP connection.

To summarize the total displacements Figure 4.11 has been generated. The total displacement is shown plotted as an absolute magnitude. Comparing the axial to the total shows little difference.

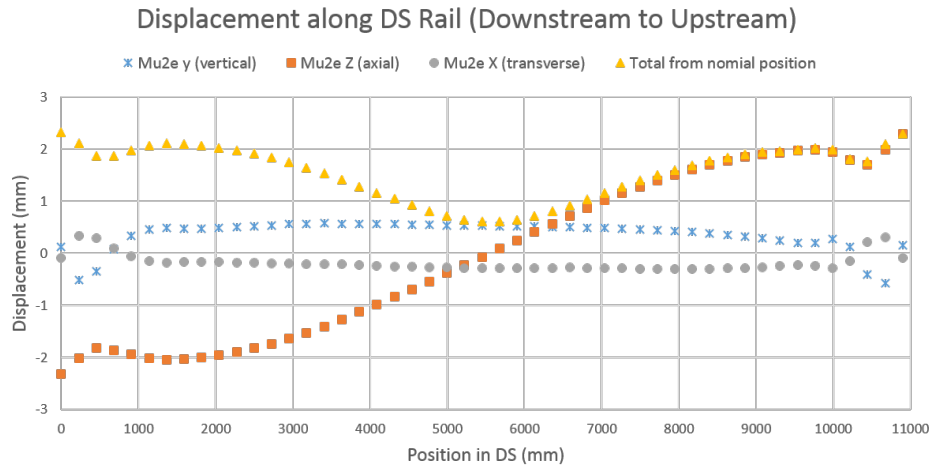


Figure 4.11: DS displacement of individual components

4.2.2.5 Stress along Rail

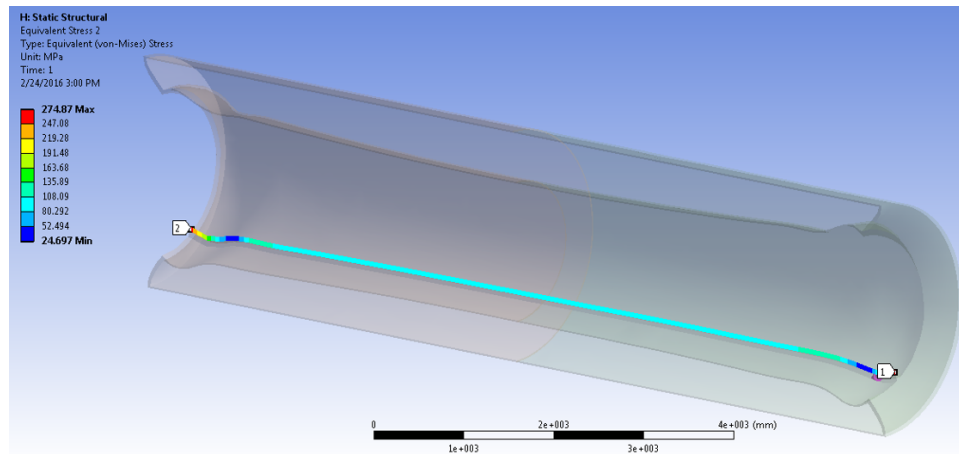
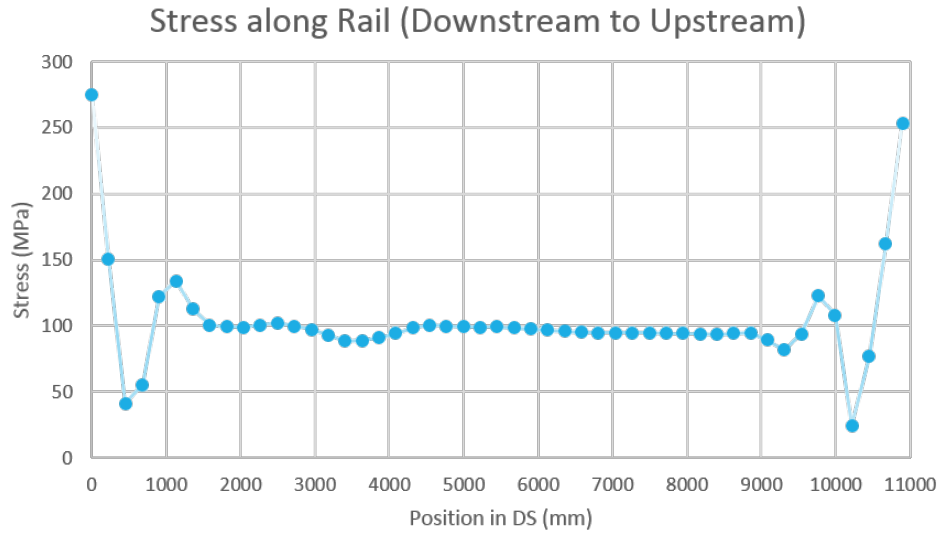


Figure 4.12: Stress along the rail from thermal contraction

As can be seen in both Figure 4.12 and 4.13, the stress that develops in the rail is significant. The peaks on both ends lie around 275 MPa which is greater than the yield stress of 248 MPa for 316L stainless steel [10]. Along the most of the rail the stress remains around 100 MPa. Even though these stresses are lower than yield, the stress due to loading

and gravitational forces have been neglected, and if included could exceed that allowed by the design. While not explicitly reported in this thesis a separate analysis was conducted that found the DS support welds yielding [16].



$$T'(x = 5.45m) = 0 \frac{^{\circ}\text{C}}{\text{m}} \quad (4.5)$$

Solving the 2nd order, linear, non-homogeneous, constant coefficient differential equation yields the following solution:

$$T(x) = 2.568x^2 - 28.0x + 20 \quad (4.6)$$

4.3.1 Comparison

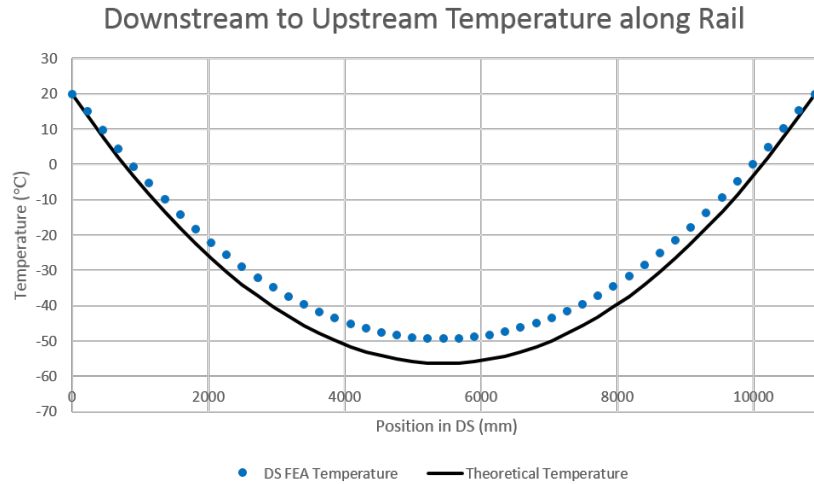


Figure 4.14: Comparison between theoretical and finite element solution

Reviewing the plot from Figure 4.14 and Equation 4.5, it can be seen that both methods have very similar results. The finite element method achieved a smaller temperature difference than the analytical solution. This was expected since the FEA model contained the rails and increased the cross-sectional area and conductive capacity of tube, whereas the simplified theoretical formulation did not. The important aspect that this plot shows is that the FEA and analytical solution curves behave in the same manner. The maximum

difference between the results over the total temperature gradient is less than 10% at the center of the tube.

4.3.2 Necessity of Temperature Control

After studying the results from the ANSYS static structural analysis, it became apparent that a need for temperature control is necessary. Introducing a new design into the pre-existing system and budget will have several implications. To meet project goals the following constraints and requirements must be considered.

4.3.2.1 Geometric Constraints

The heating equipment for the DS bore must be able to fit into a small space. The DS consists of two concentric tubes and the inner diameter of the inside tube will be the area available for a heating system. Other components also exist inside the warm bore and any additional components must not interfere with the previously allocated space.

In Figure 4.15, the outer diameters of each component is shown. Note that the outer diameters do not explicitly establish the radial constraints since several of the components have cooling and electrical lines that will exist outside of their maximum radius. Since all of the depicted components are not final designs, the cabling and consequently the routing has not been determined yet. However, current estimates state that the area to be avoided could reach but not exceed 1820 mm in diameter. Since the inner diameter of the bore is toleranced to be 1900 mm at minimum, the available area for heating equipment is between 1820 and 1900 mm.

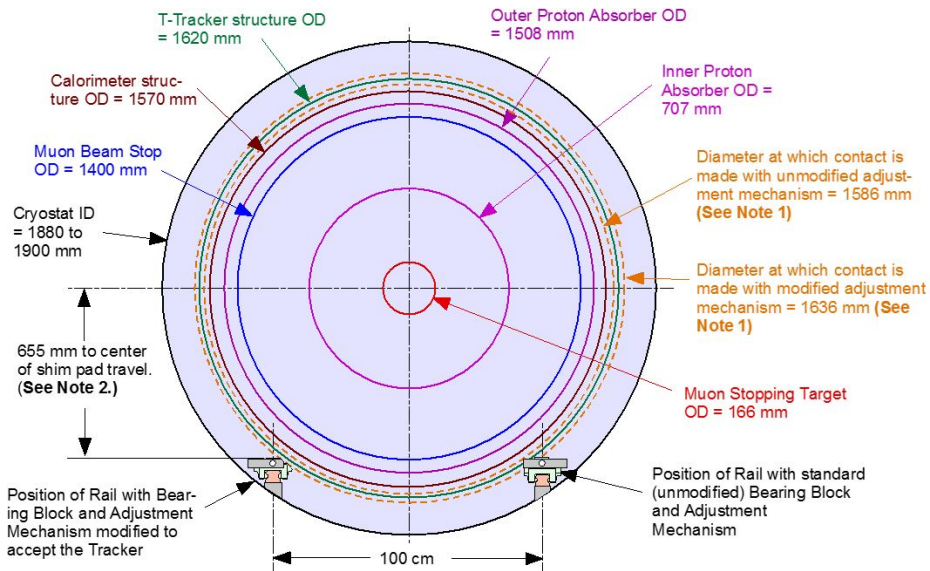


Figure 4.15: Cross-sectional view of the DS [11]

4.3.2.2 Magnetic Constraints

The heating system will exist within a magnetic field that ranges between 1T and 2T. An inherent trait of superconducting magnets is the phenomena of a quench. A quench occurs when a local area on the magnet ceases to be superconducting. This causes a rapid change in the magnetic field. To avoid the development of eddy currents, complete loops of electrically conductive materials cannot be made around the warm bore.

4.3.2.3 Temperature Requirements

Prior to completing a thermal analysis the baseline requirement for the allowable temperature range inside the DS bore was $22^{\circ}\text{C} \pm 10^{\circ}\text{C}$. This range was chosen because it stays above freezing and reduces the deflection from thermal contraction.

4.3.3 Preliminary Passive Heating System Finite Element

Analysis

Two methods of controlling the temperature in the DS are currently being pursued. A Fermilab engineer is currently exploring the possibility of using polyimide thermofoil heaters that requires feedback and temperature sensors. Alternatively, the system studied in this thesis is passive and does not require additional attention once installed. The best method to increase that temperature at the center of the DS is to increase the thermal conductivity in the axial direction. The approach used in this analysis is mounting copper bars to the warm bore. Since copper has a thermal conductivity $k=400 \frac{W}{mK}$, much greater than stainless steel, the effective thermal conductivity in the axial direction will be increased.

4.3.3.1 Copper Geometry

In this analysis 8 copper bars with a 6 inch length and 0.75 inch thickness have been added axially and spaced 45 degrees apart. To fabricate such bars, a bending method would be applied to achieve a contour that matched that of the DS. To physically connect the bars to the bore it is likely that brazing would be the chosen method.

4.3.3.2 Thermal Boundary Conditions

The boundary conditions applied to this system are identical to those of the 2D case. As can be seen in Figure 4.17, the only difference between this and the previous analysis is the presence of copper bars.

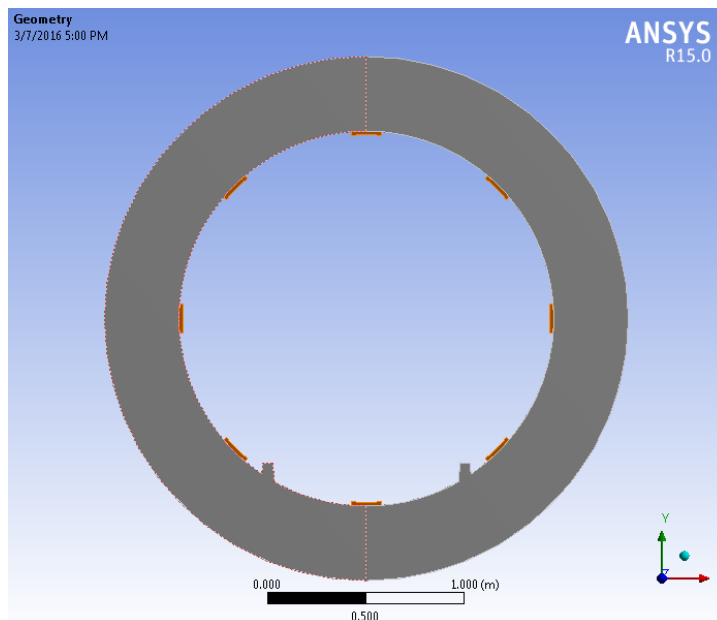


Figure 4.16: Geometry of with copper bars

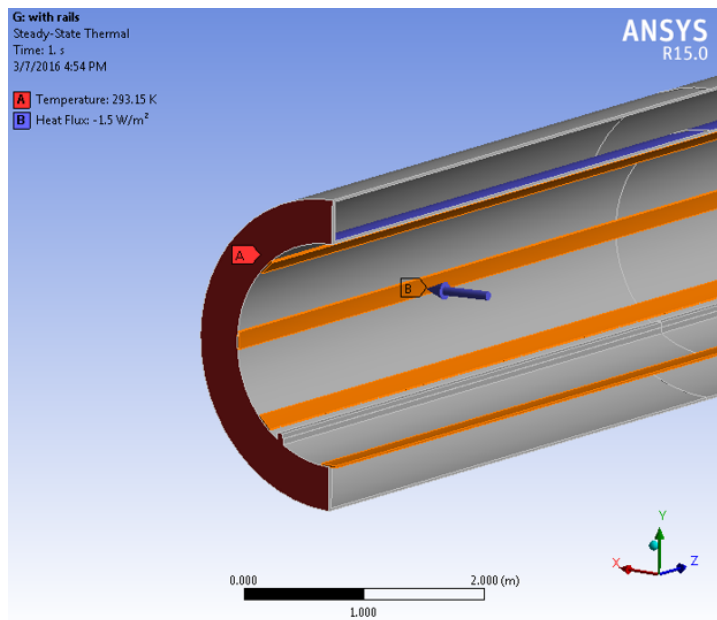


Figure 4.17: Thermal boundary conditions

4.3.3.3 Temperature Distribution

The resulting temperature difference by adding the copper bars has gone from 70°C to 12°C. Assuming that the temperature difference between end and center remained to be 12°C regardless of the temperature at the end of the DS. The outside of the DS could be held to a temperature of 25°C or greater, and the copper bar method would meet the original constraints of the design.

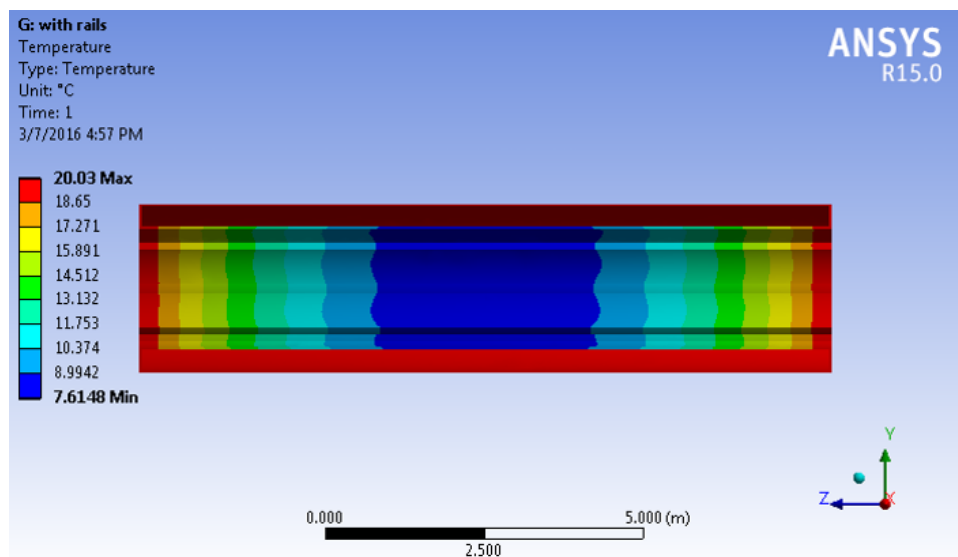


Figure 4.18: Temperature distribution with copper bars

4.4 Design Status Summary

The design of a passive heating system has been conceptualized and analysed. Future pursuits will require a more in depth study of potential heat leaks in the system. At this point in time, design alternatives and modifications are under consideration. However, it is apparent that some method of temperature control either active or passive will be required.

The proposed copper bar solution is viable under current constraints and will play a role in the development of the final system.

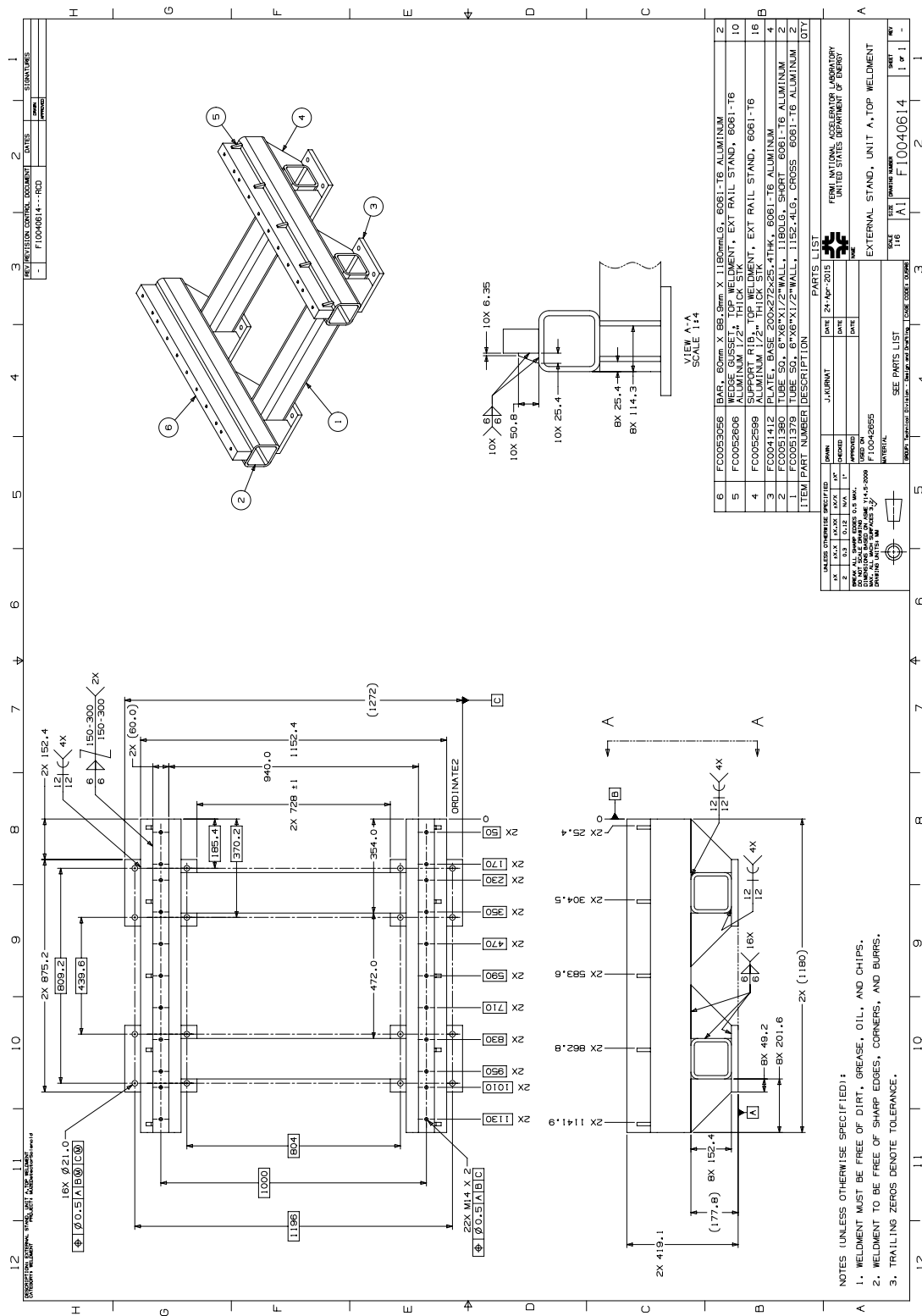
REFERENCES

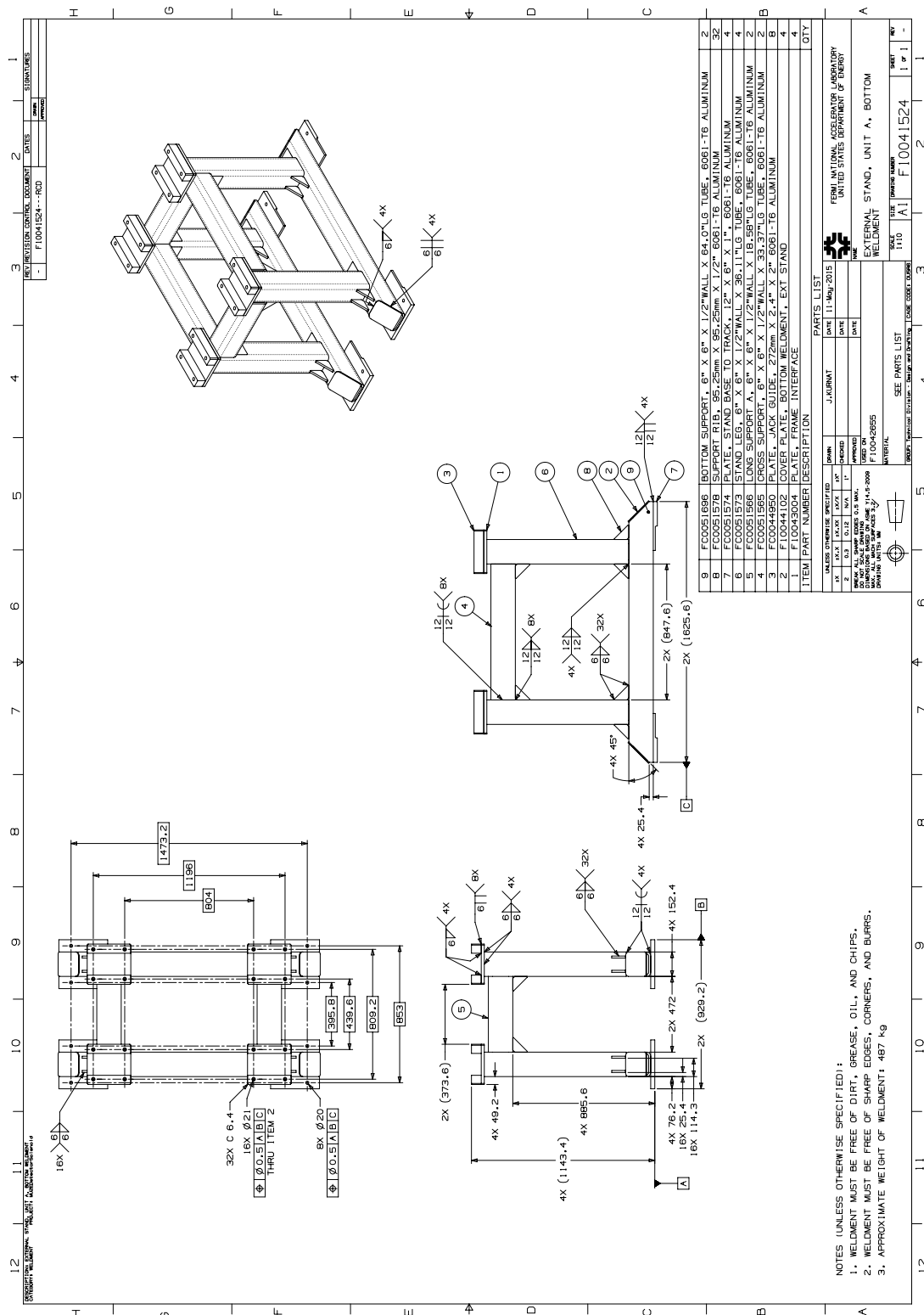
- [1] Fermi National Accelerator Laboratory, 2015, *Mu2e: muon-to-electron-conversion experiment* <http://mu2e.fnal.gov/>
- [2] MissMJ., 2014, “Standard Model of Elementary Particles,” https://commons.wikimedia.org/wiki/File:Standard_Model_of_Elementary_Particles.svg
- [3] Brown, D., 2014, “The Mu2e Experiment,” *Fermilab*, Mu2e-doc-4519-v2.
- [4] Fermilab Visual Media Services, 2015, “Fermilab Accelerator Complex,” <http://vms.fnal.gov/asset/detail?recid=1821676>
- [5] Ray, R., 2015, “Mu2e Technical Design Report (TDR),” *Fermilab*, Mu2e-doc-4299-v15.
- [6] Lamm, M., “mu2e Solenoids presentation October 29 2010,” *Fermilab*, Mu2e-doc-1142-v2.
- [7] Lamm, M., 2014, “Mu2e Transport Solenoid Requirements Document,” *Fermilab*, Mu2e-doc-947-v1.
- [8] Lamm, M., 2013, “Mu2e Dector Solenoid Requirements Document,” *Fermilab*, Mu2e-doc-946-v16.
- [9] Pronskikh, V., 2016, “MARS15 update: toward understanding the discrepancies,” *Fermilab*, Mu2e-doc-6903-v1.
- [10] Bossert, R., Martin, L., Okafor, U., Pohlman, N., 2014, “Requirements & Specifications for WBS 5.8-Muon Beam Stop,” *Fermilab*, Mu2e-doc-1351-v6.
- [11] Bossert, R., 2014, “Requirements & Specifications for WBS 5.10-Detector Support and Installation System,” *Fermilab*, Mu2e-doc-1383-v5.
- [12] Martin, L., 2016, “DS Train Installation Force Estimates,” *Fermilab*, Mu2d-doc-7100-v1.
- [13] The Aluminum Association., 2010, “Aluminum Design Manual: 2010,” Washington, D.C.
- [14] Budynas, R., Nisbett, J., and Shigley, J., 2011, “Shigley’s Mechanical Engineering Design,” McGraw-Hill, New York, NY, Chap. 3.

[15] THK Co. LTD, “Catalog No. 500-5E,” Japan.

[16] Page, T., 2016, Engineer at Fermilab, Batavia, IL., private communication.

APPENDIX
EXTERNAL STAND DRAWINGS





REV	DATE	BY	CHKD	DESCRIPTION
1	11/04/2015	ROD		EXTERNAL STAND

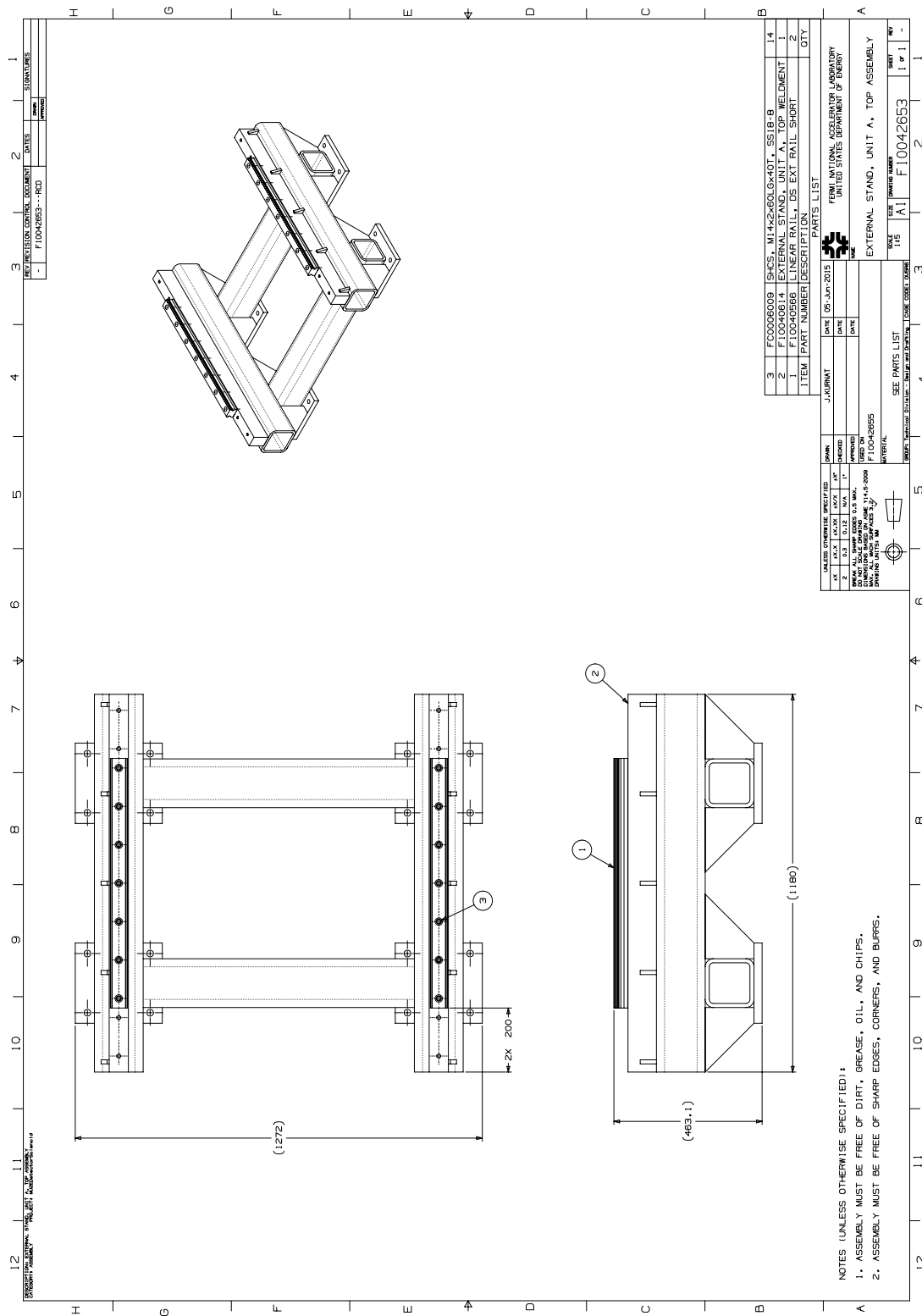
ITEM	PART NUMBER	DESCRIPTION	QTY
1	F 10043004	PLATE, FRAME INTERFACE	4
2	F 10041102	COVER PLATE, BOTTOM WELDMENT, EXT STAND	4
3	FC0043955	PLATE, SUPPORT, 6" X 6" X 1/2" WALL X 36.1" LG TUBE, 6061-T6 ALUMINUM	2
4	FC0051574	LONG SUPPORT A, 6" X 6" X 1/2" WALL X 18.5" PLUG TUBE, 6061-T6 ALUMINUM	2
5	FC0051573	STAND LEG, 6" X 6" X 1/2" WALL X 36.1" LG TUBE, 6061-T6 ALUMINUM	4
6	FC0051574	PLATE, STAND BASE TO TRACK, 12" X 6" X 1/2" WALL X 1.2" 6061-T6 ALUMINUM	32
7	FC0051578	SUPPORT RIB, 95.25mm X 95.25mm X 1.2" 6061-T6 ALUMINUM	4
8	FC0051574	PLATE, STAND BASE TO TRACK, 12" X 6" X 1/2" WALL X 1.2" 6061-T6 ALUMINUM	32
9	FC0051578	SUPPORT RIB, 95.25mm X 95.25mm X 1.2" 6061-T6 ALUMINUM	32

NAME		DATE
DESIGNED BY	J. JARONAT	11/09/2015
DRAWN BY		
CHECKED BY		
APPROVED BY		

MATERIAL	
6061-T6 ALUMINUM	1110
WELDMENT	A1

PARTS LIST	
SEE PARTS LIST	F 10041524
EXTERNAL STAND, UNIT A, BOTTOM WELDMENT	

NOTES (UNLESS OTHERWISE SPECIFIED):
 1. WELDMENT MUST BE FREE OF DIRT, GREASE, OIL, AND CHIPS.
 2. WELDMENT MUST BE FREE OF SHARP EDGES, CORNERS, AND BURRS.
 3. APPROXIMATE WEIGHT OF WELDMENT: 487 kg



ITEM	PART NUMBER	DESCRIPTION	QTY
3	FC009009	SHCS - M14x260, Gx40T, S518-B	14
2	F10040614	EXTERNAL STAND, UNIT A, TOP WELDMENT	1
1	F10040666	LINEAR RAIL, DS EXT RAIL SHORT	2

DATE	BY	DESCRIPTION
10-JUN-2015	J. GORNET	REVISED

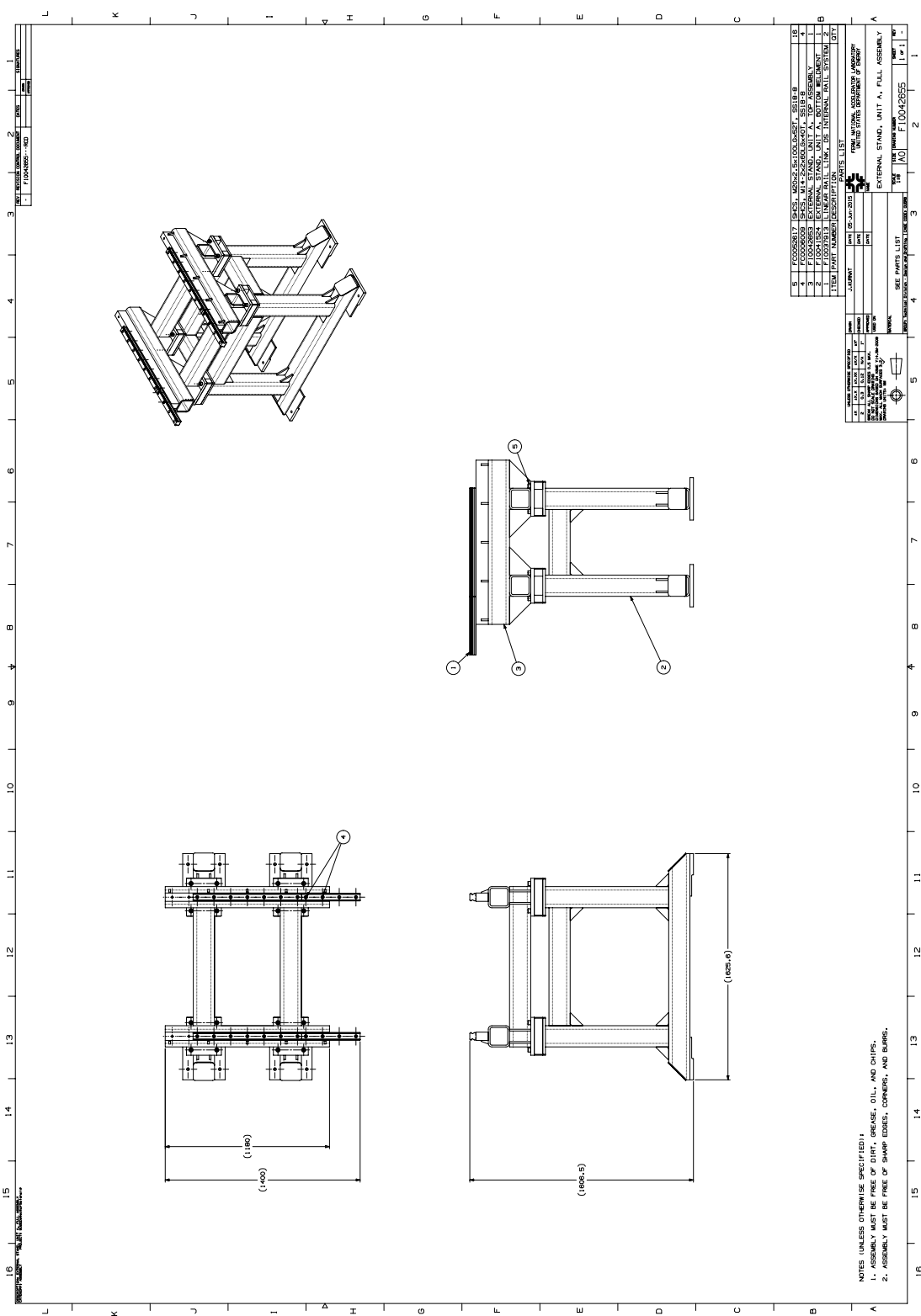
NO.	DATE	BY	DESCRIPTION
1	10-06-2015	J. GORNET	ISSUED FOR MANUFACTURE
2	03-12-2014	M. A. W.	ISSUED FOR MANUFACTURE
3	03-12-2014	M. A. W.	ISSUED FOR MANUFACTURE
4	03-12-2014	M. A. W.	ISSUED FOR MANUFACTURE
5	03-12-2014	M. A. W.	ISSUED FOR MANUFACTURE
6	03-12-2014	M. A. W.	ISSUED FOR MANUFACTURE
7	03-12-2014	M. A. W.	ISSUED FOR MANUFACTURE
8	03-12-2014	M. A. W.	ISSUED FOR MANUFACTURE
9	03-12-2014	M. A. W.	ISSUED FOR MANUFACTURE
10	03-12-2014	M. A. W.	ISSUED FOR MANUFACTURE
11	03-12-2014	M. A. W.	ISSUED FOR MANUFACTURE
12	03-12-2014	M. A. W.	ISSUED FOR MANUFACTURE

UNLESS OTHERWISE SPECIFIED:
 1. ASSEMBLY MUST BE FREE OF DIRT, GREASE, OIL, AND CHIPS.
 2. ASSEMBLY MUST BE FREE OF SHARP EDGES, CORNERS, AND BURRS.

SEE PARTS LIST
 MATERIAL
 115 A1 F10042653
 SCALE: 1:1

EXTERNAL STAND, UNIT A, TOP ASSEMBLY
 FERMILAB NATIONAL ACCELERATOR LABORATORY
 UNITED STATES DEPARTMENT OF ENERGY

12 11 10 9 8 7 6 5 4 3 2 1
 H G F E D C B A
 REVISIONS
 DATE BY
 F10042653-1000

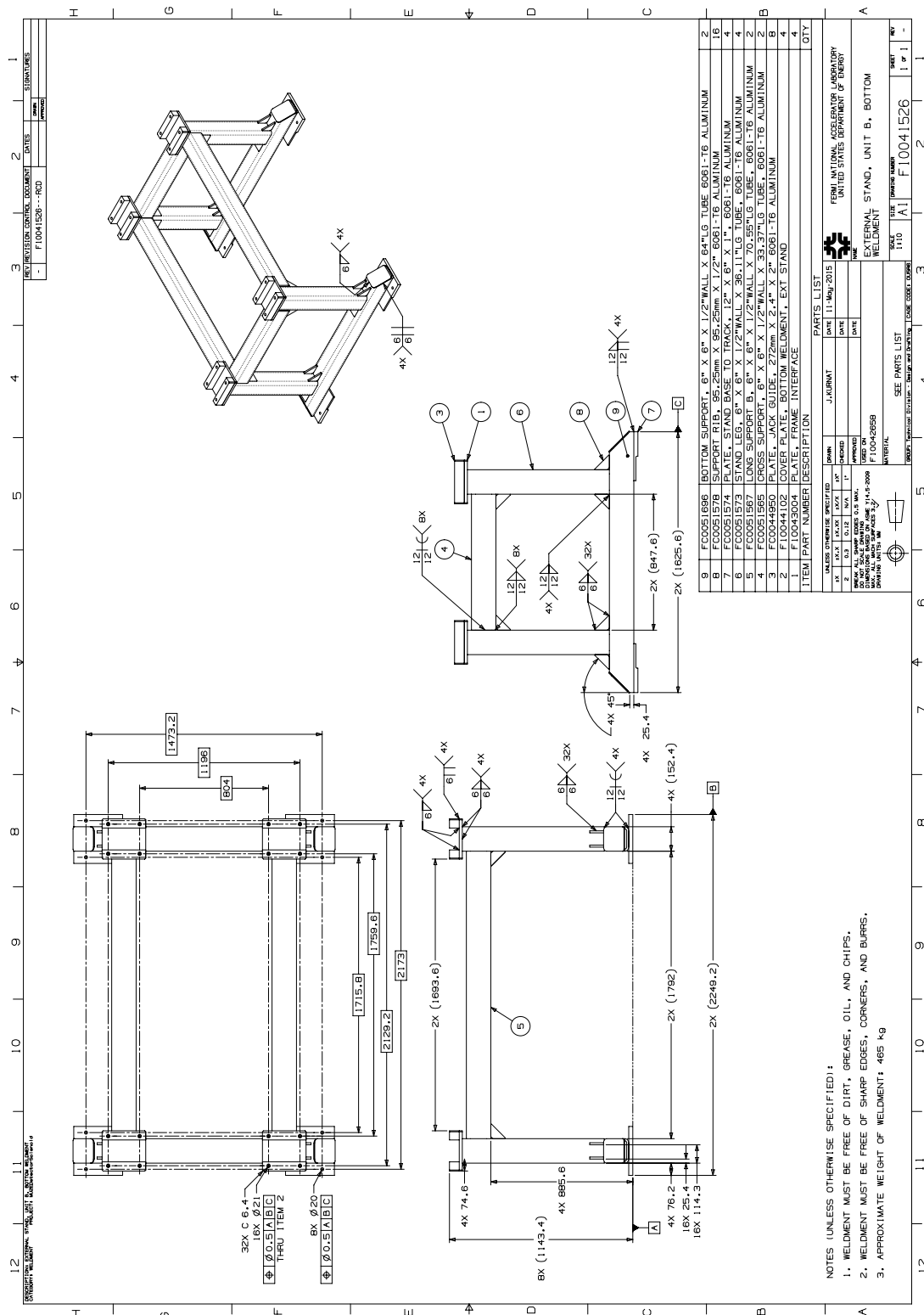


REV	DATE	BY	CHKD	DESCRIPTION
1	05-JAN-2013			EXTERNAL STAND UNIT A, FULL ASSEMBLY
2				EXTERNAL STAND UNIT A, FULL ASSEMBLY
3				EXTERNAL STAND UNIT A, FULL ASSEMBLY
4				EXTERNAL STAND UNIT A, FULL ASSEMBLY
5				EXTERNAL STAND UNIT A, FULL ASSEMBLY
6				EXTERNAL STAND UNIT A, FULL ASSEMBLY
7				EXTERNAL STAND UNIT A, FULL ASSEMBLY
8				EXTERNAL STAND UNIT A, FULL ASSEMBLY
9				EXTERNAL STAND UNIT A, FULL ASSEMBLY
10				EXTERNAL STAND UNIT A, FULL ASSEMBLY
11				EXTERNAL STAND UNIT A, FULL ASSEMBLY
12				EXTERNAL STAND UNIT A, FULL ASSEMBLY
13				EXTERNAL STAND UNIT A, FULL ASSEMBLY
14				EXTERNAL STAND UNIT A, FULL ASSEMBLY
15				EXTERNAL STAND UNIT A, FULL ASSEMBLY
16				EXTERNAL STAND UNIT A, FULL ASSEMBLY

NOTES UNLESS OTHERWISE SPECIFIED:
 1. ASSEMBLY MUST BE FREE OF BURR, BRUISE, OIL, AND DIRT.
 2. ASSEMBLY MUST BE FREE OF SHARP EDGES, CORNER, AND BURRS.

ITEM	QTY	DESCRIPTION
1	1	EXTERNAL STAND UNIT A, FULL ASSEMBLY
2	1	EXTERNAL STAND UNIT A, FULL ASSEMBLY
3	1	EXTERNAL STAND UNIT A, FULL ASSEMBLY
4	1	EXTERNAL STAND UNIT A, FULL ASSEMBLY
5	1	EXTERNAL STAND UNIT A, FULL ASSEMBLY
6	1	EXTERNAL STAND UNIT A, FULL ASSEMBLY
7	1	EXTERNAL STAND UNIT A, FULL ASSEMBLY
8	1	EXTERNAL STAND UNIT A, FULL ASSEMBLY
9	1	EXTERNAL STAND UNIT A, FULL ASSEMBLY
10	1	EXTERNAL STAND UNIT A, FULL ASSEMBLY
11	1	EXTERNAL STAND UNIT A, FULL ASSEMBLY
12	1	EXTERNAL STAND UNIT A, FULL ASSEMBLY
13	1	EXTERNAL STAND UNIT A, FULL ASSEMBLY
14	1	EXTERNAL STAND UNIT A, FULL ASSEMBLY
15	1	EXTERNAL STAND UNIT A, FULL ASSEMBLY
16	1	EXTERNAL STAND UNIT A, FULL ASSEMBLY

EXTERNAL STAND UNIT A, FULL ASSEMBLY
 PART NUMBER: F10042955
 DATE: 05-JAN-2013
 DRAWN BY: [Name]
 CHECKED BY: [Name]
 APPROVED BY: [Name]



ITEM	PART NUMBER	DESCRIPTION	QTY
9	FC0051568	BOTTOM SUPPORT, 6" X 6" X 1/2" WALL X 8471.6 TUBE 6061-T6 ALUMINUM	2
8	FC0051578	SUPPORT RIB, 95.25mm X 1.2" 6061-T6 ALUMINUM	16
7	FC0051574	PLATE, STAND BASE TO TRACK, 12" X 6" X 1/4" 6061-T6 ALUMINUM	4
6	FC0051573	STAND LEG, 6" X 6" X 1/2" WALL X 36.11" LG TUBE, 6061-T6 ALUMINUM	4
5	FC0051567	LONG SUPPORT B, 6" X 6" X 1/2" WALL X 70.5" LG TUBE, 6061-T6 ALUMINUM	2
4	FC0044355	LONG SUPPORT A, 6" X 6" X 1/2" WALL X 70.5" LG TUBE, 6061-T6 ALUMINUM	2
3	FC0044355	LONG SUPPORT C, 6" X 6" X 1/2" WALL X 70.5" LG TUBE, 6061-T6 ALUMINUM	2
2	F10044102	COVER PLATE, BOTTOM WELDMENT, EXT STAND	4
1	F10043904	PLATE, FRAME INTERFACE	4

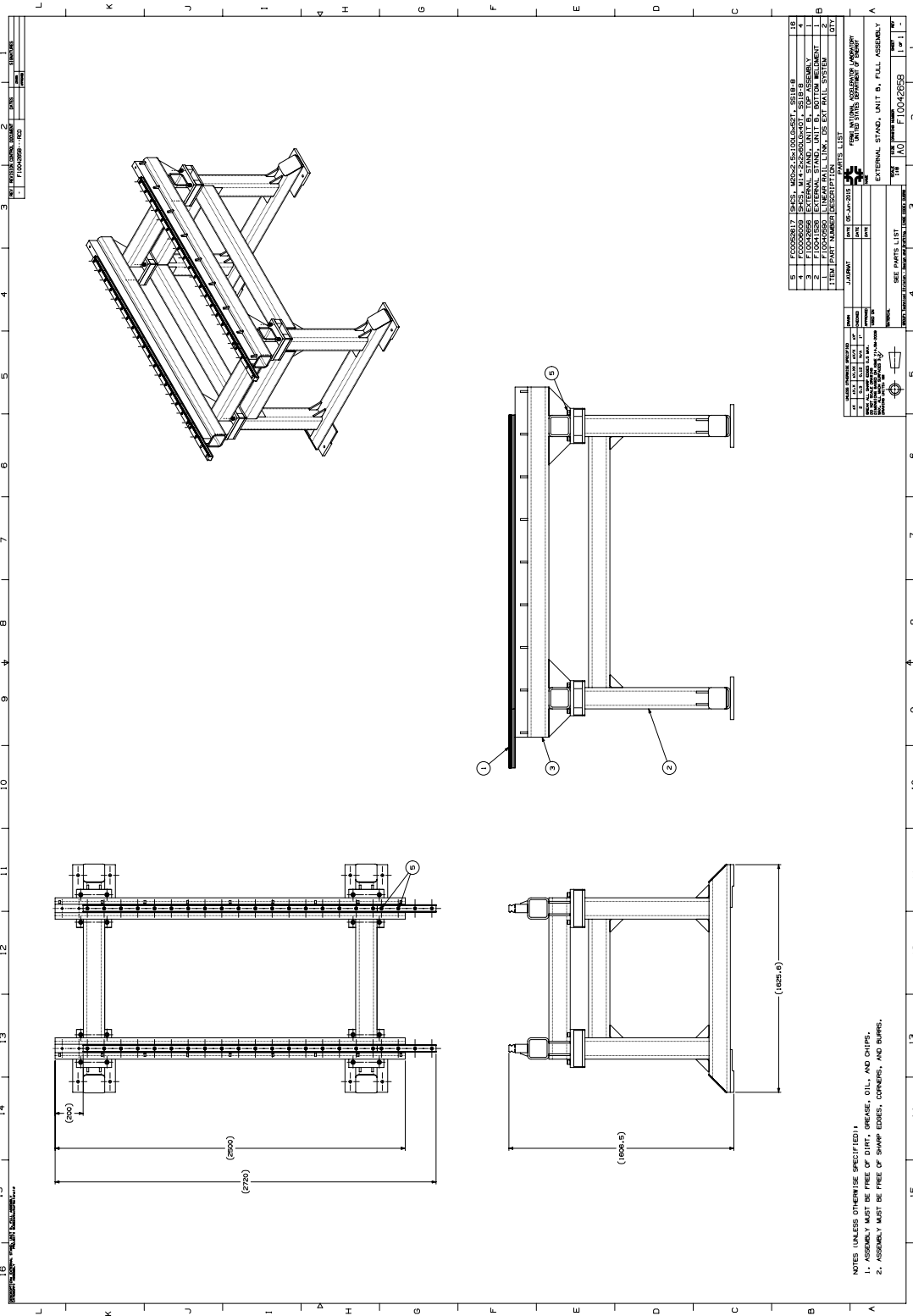
NOTES (UNLESS OTHERWISE SPECIFIED):
 1. WELDMENT MUST BE FREE OF DIRT, GREASE, OIL, AND CHIPS.
 2. WELDMENT MUST BE FREE OF SHARP EDGES, CORNERS, AND BURRS.
 3. APPROXIMATE WEIGHT OF WELDMENT: 465 kg

DATE	BY	CHKD	APP'D
11/09/2015	J. J. J.		

FERM NATIONAL ACCELERATOR LABORATORY
 UNITED STATES DEPARTMENT OF ENERGY

EXTERNAL STAND, UNIT B, BOTTOM WELDMENT

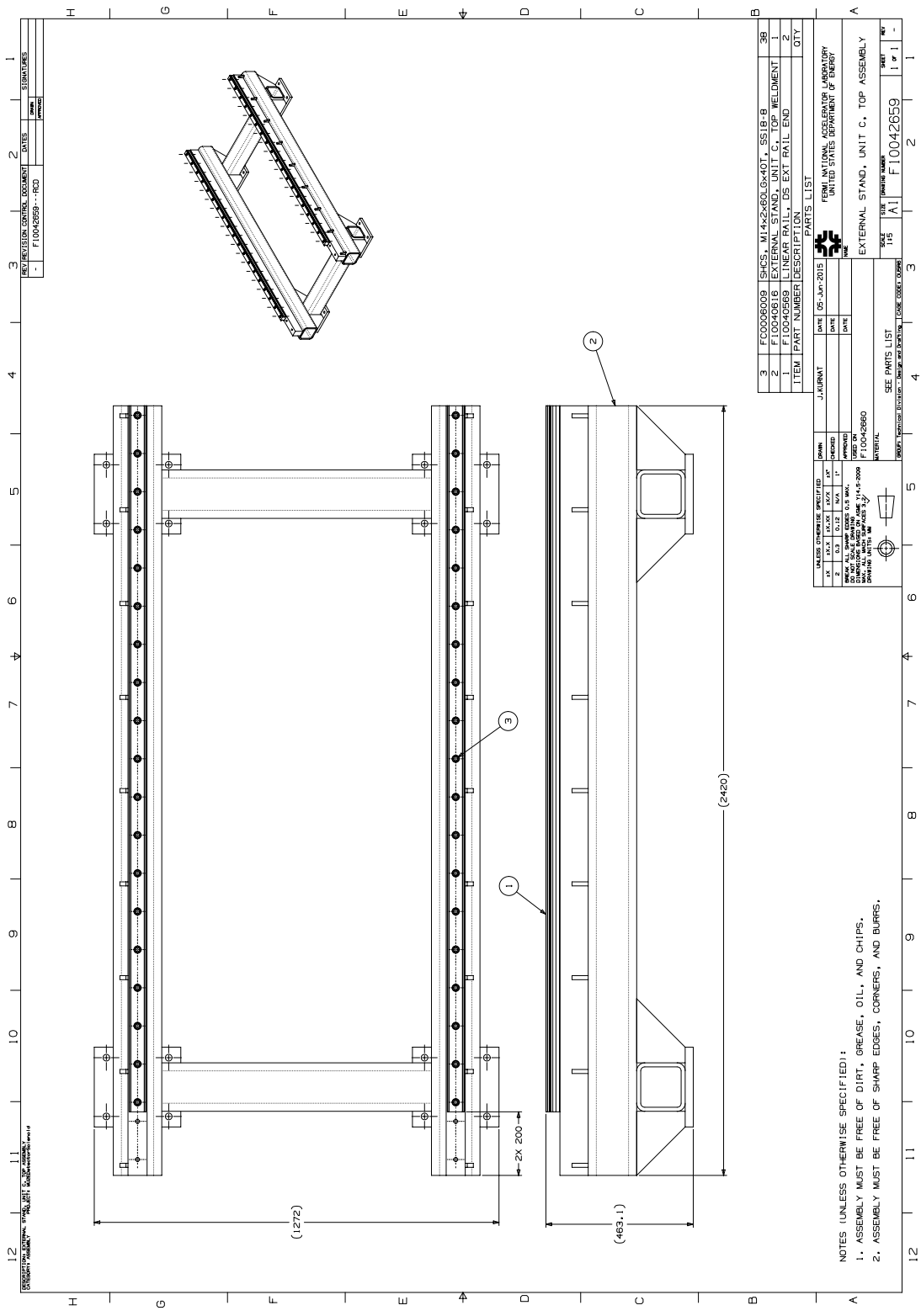
SCALE: 1:1
 SHEET: 1 of 1



EXTERNAL STAND, UNIT B, FULL ASSEMBLY		REV	DATE	BY	CHKD
1	EXTERNAL STAND, UNIT B, FULL ASSEMBLY	1			
2	EXTERNAL STAND, UNIT B, FULL ASSEMBLY	1			
3	EXTERNAL STAND, UNIT B, FULL ASSEMBLY	1			
4	EXTERNAL STAND, UNIT B, FULL ASSEMBLY	1			
5	EXTERNAL STAND, UNIT B, FULL ASSEMBLY	1			

EXTERNAL STAND, UNIT B, FULL ASSEMBLY		REV	DATE	BY	CHKD
1	EXTERNAL STAND, UNIT B, FULL ASSEMBLY	1			
2	EXTERNAL STAND, UNIT B, FULL ASSEMBLY	1			
3	EXTERNAL STAND, UNIT B, FULL ASSEMBLY	1			
4	EXTERNAL STAND, UNIT B, FULL ASSEMBLY	1			
5	EXTERNAL STAND, UNIT B, FULL ASSEMBLY	1			

NOTES (UNLESS OTHERWISE SPECIFIED):
 1. ASSEMBLY MUST BE FREE OF DIRT, GREASE, OIL, AND CHIPS.
 2. ASSEMBLY MUST BE FREE OF SHARP EDGES, CORNERS, AND BURRS.



ITEM	PART NUMBER	DESCRIPTION	QTY
3	F0006009	SHCS - M14x260, Gx40T - SS18-8	38
2	F10040616	EXTERNAL STAND, UNIT C, TOP WELDMENT	2
1	F10040669	LINEAR RAIL, DS EXT RAIL END	2

PARTS LIST

DATE	BY	DESCRIPTION
10-20-2015	J. KERNAT	REVISED

FERMI NATIONAL ACCELERATOR LABORATORY
UNITED STATES DEPARTMENT OF ENERGY

- NOTES (UNLESS OTHERWISE SPECIFIED):
- ASSEMBLY MUST BE FREE OF DIRT, GREASE, OIL, AND CHIPS.
 - ASSEMBLY MUST BE FREE OF SHARP EDGES, CORNERS, AND BURRS.

